Plagioclase preferred orientation in layered mylonites: Evaluation of flow laws for the lower crust

by
Luc Mehl

M.S., Geology, University of California, Santa Barbara, 2003
B.S., Geology, Carleton College, 2000

Submitted in partial fulfillment of the requirements of the degree of
Master of Science
at the
MASSACHUSETTS INSTITUTE OF TECHNOLOGY
and the
WOODS HOLE OCEANOGRAPHIC INSTITUTION

February 2008

Signature of Author:

Joint Program in Marine Geology and Geophysics
Massachusetts Institute of Technology
and Woods Hole Oceanographic Institution
January 18, 2008

Certified by:

Greg Hirth
Associate Professor
Thesis Supervisor

Accepted by:

Bradford Hager
Cecil and Ida Green Professor of Earth Sciences
Chair, Joint Committee for Geology and Geophysics
Massachusetts Institute of Technology
and Woods Hole Oceanographic Institution

Plagioclase preferred orientation in layered mylonites: Evaluation of flow laws for the lower crust

by
Luc Mehl

Submitted to the Department of Marine Geology and Geophysics on January 18, 2008 in Partial Fulfillment of the Requirements for the Degree of Master of Science in Geophysics

Abstract
We evaluate the applicability of plagioclase and gabbro flow laws by comparing predicted and observed deformation mechanisms in gabbroic shear zones. Gabbros and layered gabbro mylonites were collected from the Southwest Indian Ridge (SWIR), ODP Hole 735B. Deformation temperatures are constrained by two-pyroxene thermometry, stress is estimated from grain size, and deformation mechanisms are analyzed by microstructure and the presence or absence of a lattice preferred orientation (LPO). Our analyses indicate that mylonite layers deformed at a strain rate in the range of 10^{-12} to 10^{-11} s^{-1}, while coarse-grained gabbro deformed at a strain rate of approximately 10^{-14} to 10^{-13} s^{-1}. Plagioclase in pure plagioclase mylonite layers exhibit strong LPOs indicating they deform by dislocation creep. Plagioclase grain size in mixed plagioclase-pyroxene mylonite layers is finer than in pure plagioclase layers, and depends on the size and proportion of pyroxenes. Progressive mixing of pyroxene and plagioclase within gabbro mylonite layers is accompanied by weakening of the LPO indicating that phase mixing promotes a transition to diffusion creep processes that involve grain boundary sliding. Our results indicate that experimental flow laws are accurate at geologic strain rates, although the strain rate for diffusion creep of fine-grained gabbro may be underestimated. At the conditions estimated for the SWIR crust, our calculations suggest that strain localization leads to a factor of two to four decrease in lower crustal viscosity. Even so, the viscosity of lower gabbroic crust is predicted to be similar to that of dry upper mantle.

Thesis Supervisor: Greg Hirth
Title: Associate Professor of Geological Sciences

1. Introduction

In this paper we analyze microstructures preserved in mylonites from the oceanic crust to evaluate the applicability of flow laws for gabbroic rocks. The rheology of gabbroic rocks controls the mechanical behavior of the lower oceanic and lower continental crust – and likely the crust of other planetary bodies [e.g., Venus; *Mackwell et al.*, 1998]. Development of a quantitative database for the rheological properties of plagioclase-rich rocks has proven particularly challenging given the complexities of albite-anorthite solid solution, the difficulty of measuring triclinic crystal orientations with a universal-stage, and the slow coupled-diffusion of NaSi ↔ CaAl [*Yund and Tullis*, 1991]. However, experimental studies completed over the last 10 years have significantly improved our understanding of both the rheology of plagioclase [e.g., *Stünitz et al.*, 2003; *Rybacki and Dresen*, 2000] and gabbroic rocks [e.g., *Mackwell et al.*, 1998; *Dimanov and Dresen*, 2005]. The flow laws determined by these experiments require significant extrapolation to natural conditions – particularly in strain rate and total strain [e.g., *Rutter*, 1999]. Comparison of observed deformation mechanisms with predictions based on extrapolation of the laboratory data provides a test on the applicability of flow laws at geologic conditions.

We analyzed gabbro mylonites collected at the Southwest Indian Ridge (SWIR) in Ocean Drilling Program (ODP) Hole 735B. The SWIR mylonites are ideal for rheological analysis because the rapid uplift, elevated geotherm, and rapid cooling of the ridge environment promote preservation of high-temperature microstructures. These factors help mitigate potential problems with the application of recrystallized grain size to constrain differential stress and using equilibrium thermodynamics to estimate temperature during deformation. In addition, previous structural and thermochronologic analyses [*John et al.*, 2004] can be used to provide independent estimates for strain rate.

The localized nature of deformation in the SWIR gabbros allows us to investigate processes responsible for strain localization. At depths below the brittle-plastic transition, strain is often localized in cm to km-scale shear zones [*Ramsay*, 1980]. Shear zones have a lower effective viscosity than the host rock and thus may significantly influence the

bulk rheological behavior of the crust. The rheology of shear zones is also important for evaluating whether the lower crust is a strong or weak layer separating the upper crust from the mantle [e.g., *Jackson*, 2002] as well as for modeling post-seismic creep [e.g., *Montesi and Hirth*, 2003; *Freed and Burgmann,* 2004]. As part of this study, we evaluate how the bulk viscosity of the crust may decrease in the presence of shear zones. In addition, the presence of monophase plagioclase and mixed plagioclase-pyroxene layers within the mylonites allows us to investigate how second phases influence grain size and the rheology of shear zones.

To identify deformation mechanisms we rely primarily on the measurement of the lattice preferred orientation (LPO) of recrystallized plagioclase. We start with the assumption that the presence of an LPO is diagnostic of dislocation creep, while a random LPO is diagnostic of diffusion creep. The basis for this assumption is that strain during dislocation creep is dominantly accommodated by glide on the easiest slip system for the material. As deformation continues, grains rotate toward orientations that promote slip on the dominant slip system [e.g., *Nicolas and Poirier*, 1976; *Urai et al.*, 1986]. By contrast, a weak or random LPO is commonly cited as evidence for diffusion creep processes. Theoretical studies illustrate that grain boundary sliding (GBS) is required during diffusion creep [*Raj and Ashby*, 1971]. Owing to variations in grain size, phase proportions, and curvature along grain boundaries, grain boundary sliding and associated grain switching [*Ashby and Verrall*, 1973] can result in relative grain rotations and thus randomize a preexisting LPO during diffusion creep.

Weak and random LPOs, as well as weakening of preexisting LPOs have been interpreted to result from deformation dominated by diffusion-accommodated grain boundary sliding [e.g., *Boullier and Gueguen*, 1975; *Schmid et al*., 1977, *Fliervoet et al*., 1997; *Fliervoet et al*., 1999; *Halfpenny et al.*, 2006; *Kruse and Stünitz*, 1999; *Jiang et al*., 2000; *Bestmann and Prior*, 2003; *Warren and Hirth*, 2006]. Similarly, randomization of misorientation angles in calcite mylonites with a strong LPO has been attributed to GBS [e.g., *Bestmann and Prior*, 2003]. The microstructures produced during formation of the SWIR mylonites – particularly phase-mixing observed in polyphase layers – allows us to

investigate the role of GBS on the development of LPO in the context of experimental constraints on the active deformation mechanisms.

2. Southwest Indian Ridge

Gabbros were collected from the Atlantis II Fracture Zone of the SWIR, 32º43'S, 57º18'E, during ODP Legs 118 and 176. The massif is interpreted as an oceanic core-complex exhumed along a shallow detachment surface [*Dick et al*., 1991; *Baines et al*., 2003]. ODP Hole 735B extends to 1508 m, with 86% recovery, nearly all of which is gabbro [*Dick et al*., 1999].

The SWIR crust is estimated to have been approximately 4 kilometers thick prior to detachment faulting. 1508 m of material was recovered from Hole 735B, and fluid inclusion studies suggest that two kilometers of crust were removed from above the massif during detachment faulting [*Vanko and Stakes*, 1991]. Seismic profiles and sampling from a submersible indicate that the base of the gabbroic section lies 200 – 600 m below the base of Hole 735B [*Muller et al*., 1997; *Dick et al*., 1999; see also *Francis and Raitt*, 1967; *Brown and White*, 1994]. Our study focuses on processes within the lower kilometer of Hole 735B, representing the middle of the lower crust (Figure 1).

SWIR gabbros are coarse grained (5 to 30 mm), equigranular or vari-textured, with an average of ~60% plagioclase with compositions of An_{50-80} in primitive gabbros and An_{29-60} in differentiated gabbros [*Bloomer et al*., 1991; *Dick et al*., 1999; *Dick et al*., 2000]. Augite is the dominant second phase, and olivine is common. Small fractions of orthopyroxene, amphibole, and biotite are present throughout the core. The Fe-Ti oxides magnetite and ilmenite compose less than 1% of the gabbros, but are concentrated in oxide-gabbro layers.

Textures indicative of crystal plastic deformation are observed at all depths in the core. 14% of the upper 500 m (ODP Leg 118) and 7% of the lower 1000 m (ODP Leg 176) are variably foliated [*Dick et al*., 1999]. Deformation fabrics are most intense in the upper 100 m of the core, near the detachment surface, but shear zones are spaced

irregularly throughout the core (Figure 1). All shear zones show layering of variably mixed plagioclase and pyroxene-rich horizons (Figure 2).

3. Methods

Oriented samples were cut perpendicular to foliation and parallel to lineation so that the thin sections contain the lineation and pole to foliation. Samples were selected based on mineralogy and recrystallization textures. Seven high-strain samples were selected for fabric analysis; four of these were used to calculate equilibrium temperatures.

3.1. Grain Size Analysis

Mean grain size was calculated using the line-intercept method for plagioclase, pyroxenes, olivine, and oxides. Intercepts were measured from cross-polarized photomicrographs taken with an optical microscope with and without a gypsum plate. At least 100 grains of each phase were measured parallel to both maximum stretching (X) and shortening (Z) directions. The arithmetic mean for each phase was calculated for the X and Z intercept measurements separately. We use the arithmetic mean rather than the geometric mean for consistency with grain size analyses on the experimental samples from which the flow law parameters were derived. Line intercepts are converted to grain size by a geometric correction factor. To facilitate comparison with plagioclase flow laws, we determine the correction factor following the procedure used to determine grain size in the experiments of *Rybacki and Dresen* 2000, which accounts for the grain aspect ratio [*Underwood*, 1970]. The SWIR mylonites have grain aspect ratios of 1.03 – 1.27, which correspond to correction factors of 1.5 – 1.6. For consistency, we multiply mean intercept lengths by a factor of 1.5 for all samples.

3.2. Thermometry

Equilibrium temperatures are calculated for clinopyroxene-orthopyroxene pairs within the recrystallized rims and/or tails of clinopyroxene porphyroclasts. Analyzed grains ranged from 15 – 200 μm in diameter. Oxide weight percents were measured in

core and rim spots between adjacent pyroxenes using a JEOL JXA-733 Superprobe (Massachusetts Institute of Technology), with a 10-µm spot size, 10-nA beam current, and an accelerating voltage of 15 kV. Two clinopyroxene-orthopyroxene pairs were analyzed in each of four thin sections. We calculate temperature based on clinopyroxene-orthopyroxene net transfer with the Ca-QUILF software [*Lindsley and Frost*, 1992; *Andersen et al*., 1993]. Calculations include forsterite activity when olivine is present.

3.3. EBSD analysis

Microprobe-polished thin sections were further polished in colloidal silica for four hours with four pounds of loading force. Thin sections were sputter coated with Au-Pd for 80 seconds. The coating was rubbed off with paper, leaving enough Au-Pd along grain boundaries and cracks to limit charging in the SEM. Crystal orientations were measured at Marine Biological Laboratory/Woods Hole Oceanographic Institution on a Jeol 840 SEM at 15 kV, beam current 60nA. Diffraction patterns were manually selected and evaluated using the HKL Channel 5+ software.

Several distinct layers were analyzed within each shear zone. Data are summarized in pole figures and are contoured using the software of David Mainprice [www.gm.univ-montp2.fr/mainprice//CareWare_Unicef_Programs] when more than 200 orientations are measured. Fabric strength is quantified following the M-index procedure of *Skemer et al.* [2005]. We also measured the misorientation axes across subgrain boundaries to constrain the active slip systems within porphyroclasts [e.g., *Kruse et al*., 2001; *Wheeler et al*., 2001].

4. Results

4.1. Microstructures

Low magnification micrographs of four shear zones are shown in Figure 2. In general, the gabbros show the following spatial variation in microstructure: *igneous textures*: undeformed coarse (5-30 mm) equi-axed plagioclase and clinopyroxene grains; *onset of deformation:* plagioclase exhibits subgrain boundaries and core-mantle textures

(a porphyroclast with variable subgrain development surrounded by small recrystallized grains), clinopyroxene has modest to no undulatory extinction; *porphyroclastic:* all phases are porphyroclastic with recrystallized tails sweeping into the shear zone; *mylonitic:* fine-grained monophase and polyphase recrystallized layers, described below.

Monophase mylonite layers: Monophase plagioclase layers are observed in all but one of the shear zones. Microstructures in lower strain regions illustrate that these layers originate from single porphyroclasts, and grain sizes are equivalent or smaller than subgrains in porphyroclasts (Figure 3). We infer that monophase layers in the highly strained regions have a similar origin. Plagioclase crystals show straight to slightly curved boundaries; the dihedral angles at three grain junctions are often ~120º (Figure 3a). Undulatory extinction is uncommon in recrystallized grains; twins are common regardless of grain size.

Polyphase mylonite layers: Shear zones typically have many polyphase layers with plagioclase content ranging from 44 to 90% (Figure 2). The pyroxenes in these layers are typically small recrystallized grains present at plagioclase grain boundaries and corners (Figure 3b). As illustrated in Figure 2, the polyphase layers originate from clinopyroxene porphyroclasts, and become more mixed with distance from the host. Grain boundaries in these layers are typically straight, while interphase boundaries are more often curved and irregular (Figure 3b).

Fe-Ti oxide gabbro mylonite layers: Oxide gabbros are common throughout the drill core and often have a well-developed foliation. The oxide content locally approaches 90%, forming an interconnected framework. Rafts of very fine-grained recrystallized plagioclase are often suspended within the oxide-dominant layers.

4.2. Grain size

Figure 4 shows grain size distributions determined using the line-intercept method within one shear zone. Mean X values are slightly larger than mean Z, with an X/Z ratio ranging from 1.03 to 1.27. The standard deviation of grain size within these samples is typically ~60 – 80% of the calculated mean. Grain size is reduced with increasing strain

and/or pyroxene abundance. Intercept lengths for all phases have log-normal distributions for both the X and Z orientations in both monophase and polyphase layers. The least symmetric lognormal distribution (clinopyroxene in 188-3.2BA, Figure 4d) corresponds to a single horizon of pyroxene within a plagioclase layer, as opposed to more distributed textures in the neighboring polyphase layers.

Grain sizes are listed in Table 1. Plagioclase grain sizes in monophase layers range from 30 – 288 μm. Plagioclase grain sizes in polyphase layers are finer grained than neighboring monophase layers, ranging from 16 to 216 μm. Pyroxene grains in the polyphase layers have 30 – 87 μm diameters. The finest grain sizes are preserved in oxide gabbro layers, where plagioclase ranges from 16 – 39 μm and oxides range from 6 – 24 μm.

4.3. Second phase pinning

Plagioclase grain size is influenced by the abundance of second phases, as evident in comparing the mean line intercepts and phase proportions in Figure 4. We observe a linear relationship between plagioclase grain size in neighboring polyphase and monophase mylonite layers, where $d_{plag\ in\ gabbro} = 0.48 d_{plag\ in\ monophase}$, $R^2 = 0.84$ (Figure 5a). The plagioclase grain size is also well described by a Zener pinning relationship with the form [e.g., *Olgaard and Evans*, 1986]:

$$d = k \frac{d_{pin}}{f^m},$$

where d is the matrix grain size, d_{pin} is the second (pinning) phase grain size (assumed to be much smaller than d), f is the volume fraction of the pinning phase, k is a proportionality constant, and the exponent m depends on the distribution of the pinning phase. A comparison of the predicted and observed grain size within polyphase layers is shown in Figure 5b. Excluding layers where $d_{plag} \approx d_{pin}$, and defining f as the total percentage of non-plagioclase phases, we find $k = 1.26$ and $m = 0.41$ ($R^2 = 0.60$). A better fit is obtained by excluding the two layers with $d_{plag}/d_{pin} < 1.5$; in this case, $k = 1.45$ and $m = 0.34$ ($R^2 = 0.83$). These values for m agree well with theory: when pinning

phases are located on grain boundaries, $m = 0.50$ [e.g., *Haroun and Budworth*, 1968]; when pinning phases resides mostly at grain corners, $m = 0.33$ [e.g., *Hellman and Hillert*, 1975]. Theoretical estimates for k range from 0.85 to 1.82, depending on whether particles reside on each boundary of a dodecahedron or at each corner of a tetrakaidecahedron, respectively [*Haroun and Budworth*, 1968; *Hellman and Hillert*, 1975]. Our results suggest that the Zener pinning relationship provides a good estimate of grain size over a large range of f (from ~15% to ~85%) and when d_{pin} is not significantly smaller than d.

4.4. Lattice Preferred Orientation

4.4.1. Plagioclase in monophase mylonite layers

The LPOs of monophase plagioclase layers are shown in Figures 6, 7, and in the appendix. Figure 6 illustrates the textures and fabrics from a single shear zone. Fabric strength and inferred slip systems for all analyzed shear zones are listed in Table 1. Pole figures for all samples in Table 1 are presented in the appendix. We follow the convention that parentheses indicate planes (hkl) and square brackets indicate axes [uvw]. The plagioclase orientations in Figure 6a show a maximum of [100] axes sub-parallel to the lineation, a maximum of poles to the (010) plane sub-parallel to the pole to foliation, and a discontinuous great circle of poles to the (001) plane. This LPO is consistent with deformation dominated by slip on the (010)[100] system. The plagioclase orientations in Figure 6b show a maximum of [100] axes subparallel to the lineation, with poles to (001) subparallel to the pole to foliation, consistent with slip on the (001)[100] system. The LPO in this layer is weaker than that in the layer from the shear zone boundary (Figure 6a, M-index of 0.07 vs. 0.18).

The relationships between recrystallized plagioclase grain orientations with respect to porphyroclasts and the shear zone boundary are shown in Figure 7. Figure 7a shows clusters of recrystallized plagioclase axes parallel to the crystallographic orientations of the plagioclase porphyroclast. Similar host-controlled relationships have been described [*Hobbs,* 1968; *Prior and Wheeler*, 1999; *Jiang et al.,* 2000]. Figure 7b

illustrates a local strain-controlled relationship for the LPO of recrystallized grains on opposite sides of a porphyroclast [c.f., *Handy*, 1990; *Bestmann et al*., 2006]. A concentration of [100] axes is observed subparallel to the local flow direction, while the maximum of (001) planes is subparallel to the porphyroclast boundary. The obliquities of the [100] maxima with respect to the porphyroclast boundary are consistent with slip on the (001)[100] system and the perturbation of flow around a rigid inclusion. The pole figures in Figure 7c (see also Figures 6a and 6b) show crystallographic orientations parallel to the shear zone boundary, which indicates that the LPO is controlled by the macroscopic shear direction.

To further investigate the slip systems active during deformation of plagioclase, we measured misorientation axes across subgrains within porphyroclasts. The misorientation axis is the crystallographic direction about which two lattice orientations can be rotated into parallelism [e.g., *Lloyd et al*., 1997; *Wheeler et al*., 2001]. Pole figures and misorientation axis plots for porphyroclasts are shown in Figure 8. The pole figures illustrate the range in subgrain orientations for the analyzed porphyroclasts — almost no spread in subgrain orientations, a 29º rotation about the (100) pole, and a spread in all three poles. The pole figure with a 29º rotation and the accompanying plot of misorientation axes suggest that the rotation between subgrains is about the (100) pole. This rotation suggests that subgrain boundaries are composed of ‘edge dislocations’ (true edge dislocation are not possible in triclinic crystals) from slip on the (010)[001] system [e.g., *Kruse et al*., 2001]. The rotation (misorientation) axes for the other porphyroclasts in Figure 8 are not as distinct, but are concentrated on the (010) plane near (100). Pole figures for other porphyroclasts are presented in the appendix Figure A3, and wherever a clear rotation axis is evident, the pole figure is consistent with rotation about the (100) axis. We conclude that (010)[001] is the dominant slip system active in development of subgrain boundaries in porphyroclasts.

In summary, the LPOs of monophase layers in the SWIR mylonites are consistent with slip on the (010)[100] and (001)[100] systems. By contrast, misorientation axes

suggest dominance of the (010)[001] dislocations during the formation of subgrain boundaries within porphyroclasts.

4.4.2. Plagioclase in polyphase mylonite layers

Pole figures for plagioclase in polyphase mylonite layers are shown in Figures 6a and 6b. In these layers, plagioclase shows no strong concentrations of crystallographic axes or poles. Weak or random fabrics (M-index of 0.04) in polyphase layers are observed throughout the sampled suite (Table 1). Fabric strength generally increases with an increase in plagioclase content (Figure 9).

4.4.3. Clinopyroxene, olivine, and Fe-Ti oxides in mylonites

Recrystallized clinopyroxene and olivine behave similarly to plagioclase in that monophase aggregates show orientation clustering (Figures 6c and 6d, see also Figures A1 and A2 in the appendix), while grains in polyphase mylonite layers are less strongly oriented (Figure 6b, and appendix). In both cases there are two few recrystallized grains to provide a robust quantification of fabric strength. Pole figures of Fe-Ti oxides in polyphase mylonite layers show random orientations (Figure A1 in the appendix).

4.5. Constraints on Deformation Conditions

4.5.1. Differential Stress

We use the empirical relationship outlined by *Twiss* [1977] to estimate stress as a function of recrystallized grain size. We modify *Twiss'* empirical relationship to reflect glide on the [100] Burgers vector for consistency with the observed LPOs. This changes the pre-exponential constant from 7.8 to 9.6. Stress estimates for monophase layers range from 20 to 100 MPa (Table 1). Ribbons of recrystallized olivine grains at the boundary of a shear zone (Figure 6d) allow us to compare the grain size/stress relationship predicted for plagioclase with two experimentally derived olivine piezometers [*Van der Wal et al.*, 1993; *Karato et al.*, 1980]. Stresses are calculated from the grain size of recrystallized olivine (see Figure 4) using a geometrical correction factor of 1.75 for consistency with

Van der Wal et al. Estimated stresses for recrystallized olivine (453 μm) are 12^{+12}_{-5} MPa using *Karato et al*.'s piezometer, and 14^{+3}_{-2} MPa using *Van der Wal et al*.'s piezometer. The neighboring monophase plagioclase stress estimate is 20 MPa. Thus, the stress estimates for olivine and plagioclase are similar.

Stress estimates based on recrystallized grain size can be misleading depending on the extent of post-deformation grain growth in addition to differences in the temperature dependence of grain growth and dislocation creep [e.g., *Austin and Evans*, 2007]. The presence of ~120º grain junctions in the monophase plagioclase layers suggests some annealing may have occurred and that stress estimates should be considered as minimum values. However, the observation that subgrain sizes are similar or somewhat larger than recrystallized grain sizes (Figure 3) suggests that post-deformation grain growth was modest.

4.5.2. Temperature

Core equilibrium temperature estimates range from 808 ± 14 to 946 ± 69 ºC; calculated temperatures are summarized in Table 2. Probe analyses are presented in Tables 3, 4, and 5. Rim temperatures are generally cooler (by 6 to 71 ºC); however the calculated temperatures of each core-rim pair are the same within the error determined with the QUILF software.

4.5.3. Strain Rate

The strain rate of the SWIR shear zones is well constrained by geologic observations. A combination of geochronology and thermal modeling of samples from 735B drill core indicates that the crust cooled from ~950 to ~800 ºC, the temperature range recorded by the mylonites, in ~200 ky [*John et al*., 2004]. The strain rate can be determined by combining the constraint on the duration of deformation with a strain estimate. Given the limited spatial sampling of the drill core, we can only determine a minimum strain estimate. Distinct shear zone layers are observed to originate from individual porphyroclasts. These layers commonly extend beyond the long dimension of

the thin section (i.e., > 20 mm), and have a thickness on the order of ~0.2 mm (e.g., Figure 2). For a porphyroclast with an initial diameter of 2 mm, a simple shear (γ) of ~10 is required to produce a recrystallized layer with dimensions of 20 mm x 0.2 mm. Given the roughly parallel orientation of the mylonitic layers with respect to the shear zone boundary, we posit that the true strain could easily be an order of magnitude greater. Given a shear strain of 10 – 100 and a deformation time of 200 ky, we calculate a shear strain rate of 2×10^{-12} s^{-1} to 2×10^{-11} s^{-1}. These shear strain rates are equivalent to axial strain rates of 10^{-12} s^{-1} to 10^{-11} s^{-1} ($\dot{\varepsilon} = \frac{\dot{\gamma}}{\sqrt{3}}$). For comparison, at a strain rate of 10^{-14} s^{-1}, a 2 mm porphyroclast would only elongate to 2.13 mm. This low magnitude of strain may be reasonable for the porphyroclasts at the shear zone boundaries, where microstructural evidence for deformation is limited to undulatory extinction in plagioclase and a small degree of recrystallization.

An additional test for the strain rate range is to calculate the strain rate for the SWIR crust assuming that the rate of spreading at the SWIR spreading center was accommodated by slip on shear zones. Approximately 10% of the drill core has high temperature deformation fabrics, giving a total shear zone thickness of ~150 meters. For a spreading rate of 14 – 16 mm/yr [*Dick et al*., 2003], the shear strain rate is in the range of 15mm yr^{-1}/150 m $\approx 3 \times 10^{-12}$ s^{-1} (equivalent axial strain rate of 2×10^{-12} s^{-1}), in agreement with our estimate based on mylonite layer geometry.

5. Discussion

Plagioclase fabrics from low and high strain gabbroic shear zones demonstrate that deformation mechanisms evolve with increasing strain. The microstructure of lower strain regions indicates that deformation is first accommodated by dislocation creep resulting in subgrain formation and the initiation of subgrain rotation recrystallization in plagioclase. In many cases, the initial orientation of recrystallized grains depends on the host orientation, as illustrated in Figures 7a and sample 149-3.2C/D in Figure A1 in the appendix. However, with increasing strain the slip planes in monophase layers rotate into

parallelism with the shear plane (i.e., the orientation becomes controlled by the shear direction, see (b) in Figure A1 in the appendix). By contrast, random fabrics or weak LPOs are observed in adjacent polyphase layers that are finer grained – suggesting a transition in the dominant deformation mechanism to diffusion creep is promoted by grain size pinning.

5.1 Microstructural Observations

5.1.1 Slip Systems

The interpretation of these fabrics is complicated by the apparent discrepancy presented by the analyses of misorientation axes in porphyroclasts and the LPO of recrystallized layers. The misorientation axis data for porphyroclasts suggest that slip on (010)[001] is easier than that on (010)[100] or (001)[100]. By contrast, the LPO of recrystallized layers suggest that slip (010)[100] and (001)[100] is easier than that on (010)[001].

Based on crystal structure, the (010)[001] slip system should be 'easy' given the large spacing between slip planes and the small spacing in the slip direction [e.g., *Marshall and McLaren*, 1977]. Indeed, dislocations and LPOs consistent with slip on (010)[001] are commonly identified in TEM of experimentally and naturally deformed plagioclase [*Olsen and Kohlstedt*, 1985; *Olesen*, 1987; *Ji and Mainprice*, 1988; *Ji et al*., 1988; *Kruse et al*., 2001; *Stünitz et al*., 2003]. However, none of the SWIR mylonite layers have LPOs consistent with slip on (010)[001].

The (010)[100] and (001)[100] systems inferred from the SWIR LPOs have also been identified in naturally and experimentally deformed plagioclase, [*Marshall and McLaren*, 1977; *Cannat*, 1991; *Siegesmund et al*., 1994; *Heidelbach et al*., 2000; *Ji et al*., 2000; *Xie et al*., 2003; *Zimmerman and Kohlstedt*, 2003; *Ji et al*., 2004]. *Ji et al*. [2000, 2004] proposed that the relative importance of the [001] or [100] Burgers vectors may be a function of temperature, strain rate, H_2O activity or confining pressure. However, within a given shear zone these parameters were presumably the same during deformation. In addition, there is no evidence that the differences in slip systems reflect

variation in composition. For example, the compositions of plagioclase in monophase layers, polyphase layers and porphyroclasts shown in Figure 6 are $An_{56\pm2}$, $An_{57\pm1}$, $An_{58\pm4}$, respectively.

Based on our results, we can only conclude that either the dominant slip systems that characterize the LPO depend on more than just the critical resolved shear stress for each slip system, or subgrain boundaries in plagioclase porphyroclasts are not dominantly composed of dislocations from the easiest slip systems. Nonetheless, it is clear that monophase plagioclase layers developed strong LPOs while finer-grained polyphase layers did not.

5.1.2 Phase Mixing and Grain Boundary Sliding

Our interpretation that deformation in the gabbro mylonites is accommodated by diffusion relies primarily on the observation of weak to random fabrics in these samples [e.g., *Lapworth et al.*, 2002]. Theoretical arguments indicate that grain boundary sliding (GBS) is required during diffusion creep [e.g., *Ashby and Verrall*, 1973]. The best evidence for grain boundary sliding (GBS) in the SWIR mylonites is the greater extent of phase mixing observed with increasing distance from clinopyroxene porphyroclasts (Figure 10). Phase mixing in the gabbro mylonites is potentially augmented by the nucleation of fine-grained pyroxenes during concomitant exsolution and dynamic recrystallization. Similar chemical driving forces have been suggested in amphibole-bearing gabbros [*Kruse and Stünitz*, 1999], quartzo-feldspathic mylonites [*Fliervoet et al.*, 1997] and peridotite mylonites [*Newman et al.*, 1999]. The observation of phase mixing together with the lack of LPO supports our interpretation that the gabbro mylonite layers deformed by diffusion creep.

5.2. Comparison of predicted and natural deformation mechanisms

We investigate relationships between LPO, second phases, and deformation mechanisms using deformation mechanism maps (DMMs) for plagioclase and gabbro. For this discussion we refer to the polyphase mylonite layers and the country rock as

gabbro mylonite and coarse-grained gabbro, respectively. The conditions where dislocation creep and diffusion creep are the dominant creep processes are calculated using experimental flow laws with the form:

$$\dot{\varepsilon} = A\sigma^n d^{-p} f_{H_2O}^r \exp^{(-Q/RT)},$$

where $\dot{\varepsilon}$ is strain rate, A is a constant, σ is stress in MPa, n is the power law exponent, d is grain size in μm, p is the grain size exponent, f_{H_2O} is water fugacity, r is the water fugacity exponent, Q is the activation enthalpy, R is the molar gas constant, and T is absolute temperature. We calculate total strain rate contours assuming that the total strain rate is the sum of the strain rate due to diffusion and dislocation creep, $\dot{\varepsilon}_{total} = \dot{\varepsilon}_{dif} + \dot{\varepsilon}_{dis}$, at temperatures of 800 and 950 ºC based on the two-pyroxene thermometry. For wet laws we set $r = 1$, as suggested by the experiments of *Rybacki et al*. [2006]; water fugacities are calculated by taking the product of water fugacity coefficients [*Tödheide*, 1972] and water fluid pressure. The value of A is then recalculated to account for the fugacity term. We assume water fluid pressure is lithostatic, and calculate the lithostatic pressure at 2500 m and 3500 m in the restored crustal section (see Figure 1) using $\rho_{rock} = 3000$ kg/m^3. We also include the load of a 4 km water column.

The experimental flow laws were all determined using uniaxial deformation experiments. We convert uniaxial strain rates to a more geologically relevant plane strain geometry assuming $\dot{\varepsilon} = \frac{\sqrt{3}}{2}\dot{\varepsilon}_{axial}$. This relationship is calculated by relating the second invariant of the strain tensors for different geometries with the assumption that the material obeys the von Mises yield criterion [*Nye*, 1953; *Jaeger and Cook*, 1969; *Schmid et al*., 1987].

Our evaluation of flow laws relies on the accuracy of our stress estimates. In addition to the evaluation of Twiss' piezometer at low stresses (Section 4.5.1), we compare our highest stress estimates with those predicted for brittle deformation mechanisms. Our calculated temperature range (800 – 950 ºC) is only slightly higher than the range suggested for the initiation of hydrothermal alteration (700 – 750 ºC, e.g.,

Manning et al., 1996; *Miranda*, 2006). Hydrothermal alteration requires a network of veins or microcracks, thus, we predict the high-stress (fine-grained) SWIR shear zones were deforming at stresses near the viscous-brittle transition.

Following *Hirth et al*. [1998], two constraints are used to determine the stress of initiation of brittle failure mechanisms. First, the differential stresses predicted for Goetze's Criteria ($\sigma_{dif} = \sigma_3$) at depths of 2500 and 3500 m (assuming σ_1 is the lithostatic pressure including the load of the water column) are 56 and 71 MPa, respectively. Goetze's Criteria provides an estimate for the stress state at the transition from semi-brittle to fully plastic flow [*Kohlstedt et al*., 1995], and thus constrains the stress below which microcracking does not occur. Second, the differential stresses predicted by Byerlee's Law [*Byerlee*, 1978] assuming a hydrostatic fluid pressure at depths of 2500 and 3500 m are 56 and 70 MPa, respectively [see also *Newman et al*., 1994]. As shown Table 1, the stresses predicted using these two constraints are in agreement with the highest stresses predicted for the SWIR mylonites using the grain size piezometer (~50-100 MPa). This agreement further supports our stress estimates and evaluation of the plagioclase and gabbro flow laws.

For completeness, we note that two other piezometers predict stresses that are inconsistent with the constraints provided by the onset of brittle deformation. The albite piezometer calibrated by *Post and Tullis* [1999] predicts stresses that fall well below the brittle-failure criteria (0.1 – 2.5 MPa). The *Post and Tullis* piezometer must be extrapolated to considerably lower stress than where it was calibrated and the recrystallization processes involved (low-temperature migration recrystallization, i.e., "bulging" recrystallization) are different than those exhibited by the SWIR samples. *Post and Tullis* emphasize that their piezometer should not be applied to rocks that exhibit evidence for either subgrain rotation or high-temperature migration recrystallization. Application of the field-boundary theory as a piezometer [e.g., *de Bresser et al*., 2001] also predicts low stresses (0.1 to 1 MPa for the samples with grain sizes of ~100 to 300 μm). This observation suggests that the piezometric grain size relationship exists independent of the field boundary hypothesis.

5.2.1. Deformation Mechanism Map for Monophase Plagioclase Layers

A deformation mechanism map for dry plagioclase is shown in Figure 11, calculated using the flow law for An_{100} [*Rybacki and Dresen*, 2000]. Monophase shear zone layers are plotted on the DMM using the stress determined from the *Twiss* piezometer. All of the monophase layers plot within the dislocation creep field, consistent with the observation that all but one layer exhibits a strong LPO. The range of differential stress estimated from the piezometry is well fit by the dry An_{100} flow law at a strain rate of 10^{-12} s^{-1}, which is consistent with the independent estimates for strain rate outlined in section 4.5.3. By contrast, extremely high strain rates of ~10^{-9} to 10^{-7} s^{-1} are predicted using the wet plagioclase flow laws for dislocation creep at the same stress and temperature range (wet anorthite An_{100} [*Rybacki and Dresen*, 2004], wet An_{60} [*Dimanov*, unpublished, in *Rybacki and Dresen*, 2004], wet Ab_{100} [*Offerhaus et al*., 2001]).

The discrepancy between the fast strain rates predicted using the flow laws for wet plagioclase and the geologically constrained rates of 10^{-12} to 10^{-11} s^{-1} suggests that H_2O activity is low during the formation of the SWIR shear zones. This result is consistent with characteristics of oceanic crust beneath spreading centers: (1) the gabbroic rocks are cumulates, so much of the water (an incompatible component) present in primitive MORB will be concentrated in the erupted lavas and (2) the crust is young, hot, and fracture free prior to the onset of brittle deformation at lower temperatures [e.g., *Hirth et al*., 1998].

5.2.2. Deformation Mechanisms for Gabbro Mylonite Layers and Coarse-Grained Gabbro

A deformation mechanism map for dry gabbro is plotted in Figure 12 using the 50An/50Cpx flow law determined for synthetic aggregates of anorthite and diopside [*Dimanov and Dresen*, 2005]. The 50An/50Cpx mixture has a volume percent ratio similar to that of the average SWIR gabbros (~60% plagioclase, 40% pyroxene and olivine). The planar banding in the layered mylonites (e.g., Figures 2 and 6), as opposed to boudinage of one layer or the other, indicates that there is little or no viscosity contrast

between plagioclase and gabbro mylonite layers. Thus, we use a strain rate of 10^{-12} s^{-1} in Figure 12 for comparison with Figure 11. The dislocation creep stresses calculated for dry and wet gabbro flow laws at various strain rates are plotted on the side in Figure 12 (50An/50Cpx and 75An/25Cpx [*Dimanov and Dresen*, 2005]; natural diabase, Mc and Mm, [*Mackwell et al*., 1998]).

Samples from the gabbro mylonite layers are plotted on Figure 12 using weighted-mean grain sizes from the gabbro layers and the stress estimated from neighboring monophase layers; therefore we assume that stress is constant between neighboring layers. The grain size for six of the seven gabbro mylonite layers that have monophase neighbors is well fit by a power law: $\sigma_d = 237d^{-0.48}$, $R^2 = 0.90$. The outlying high-stress sample was not included in the fit because it has a texturally unique interconnected oxide network. This "polyphase piezometer" suggests that second phase pinning results in a systematic change in the grain size piezometer. This result is reasonable given that the grain size of the plagioclase depends on the recrystallized grain size of the pinning phase, which also depends on differential stress. One shear zone has no monophase layer and its two gabbro layers are plotted on the "polyphase piezometer" in Figure 12.

Similar to the result for monophase layers, the gabbro mylonite samples generally plot within the stress range predicted for a temperature range of 800 – 950 ºC at a strain rate of 10^{-12} s^{-1}. Furthermore, the samples plot within the diffusion creep field or near the boundary between the two creep mechanisms. Comparison of the gabbro DMM with the monophase DMM illustrates that the temperature contours for the diffusion creep field are the same within error. However, the boundary between the diffusion and dislocation creep fields is shifted toward larger grain sizes and greater stresses. This indicates that a relative enhancement of diffusion creep occurs because dislocation creep of gabbro is inhibited relative to anorthite. However, the lowest stress (i.e., largest grain size) samples in Figure 12 still plot within the dislocation creep field despite the fact that they exhibit no LPO (M-index = 0.4). These observations suggest that the gabbro flow law underestimates the strain rate for diffusion creep.

The relationships between our deformation mechanism observations and the gabbro flow laws are further illustrated by analyzing stress-strain rate curves in Figure 13. In evaluating Figure 13, we need to account for four criteria based on our observations. (1) The strain rate predicted for the mylonites should match the geologically constrained range of 10^{-12} to 10^{-11} s^{-1}. (2) The strain rates for the plagioclase and gabbro mylonite layers should be similar. (3) The plagioclase layers should deform by dislocation creep while the gabbro layers should deform by diffusion creep. (4) The gabbro mylonite layers should deform at a much greater rate than the coarse-grained gabbro.

Figure 13 compares stress-strain rate relationships for anorthite, fine-grained gabbro, and coarse-grained gabbro at 875 ºC and 925 ºC. For a temperature of 875 ºC (i.e., the middle of our estimated temperature range) we assign grain sizes based on averages of the grain sizes illustrated in Figures 11 and 12: 100 μm for the dry anorthite flow law and 35 μm for the dry gabbro (50An/50Cpx) flow law. At 925 ºC (the temperature estimated for the coarsest-grained samples) we assign grain sizes based on the lowest stress shear zone sample: an anorthite grain size of 300 μm and a gabbro grain size of 100 μm. The behavior of coarse gabbro, outside the shear zones, is also plotted at both temperatures. We use the 50An/50Cpx flow law and a grain size of 3000 μm for the coarse gabbro.

As illustrated in Figure 13a, all four criteria are met within error of the flow laws at a temperature of 875 ºC and a stress near 50 MPa, although the strain rate predicted for the gabbro mylonite falls at the lower bound of the estimated range. The implications of Figure 13a are emphasized by considering the behavior at higher or lower stress. At lower stress, the predicted strain rate for the mylonites falls below the geologically estimated range. At higher stress, the contrast in strain rate between the gabbro mylonite and coarse gabbro diminishes. Thus, the agreement between the observed deformation mechanisms, estimated strain rates and predictions of the flow laws is limited to differential stress values approximately the same as determined by the grain size piezometry. This result arises because of the difference in the stress dependence for creep

mechanisms predicted for the gabbro mylonite (n = 1, diffusion creep) and the plagioclase mylonite (n = 3, dislocation creep).

As illustrated in Figure 13b, the same four criteria are not met at the lower stress conditions at 925 ºC. The diffusion creep strain rate for the gabbro mylonite is too low relative to that of anorthite except at stresses ≤ 5 MPa, at which point the predicted strain rates are both significantly below the geologically estimated range. At stresses ≥ 50 MPa the strain rate of the gabbro mylonite and coarse gabbro become similar because the gabbro mylonite is predicted to deform by dislocation creep, which is inconsistent with our microstructural observations. All four criteria would be met at the stress predicted by grain size piezometry (~20 MPa) if the diffusion creep strain rate for the gabbro mylonite is enhanced by approximately an order of magnitude.

While these observations indicate possible problems with the application of diffusion creep flow laws for gabbro mylonites, the rheology of the coarse gabbro is well predicted by the dislocation creep flow law. For the stress range estimated by the recrystallized grain size piezometry, the dislocation creep flow law for coarse gabbro predicts strain rates in the range of 10^{-14} to 10^{-13} s^{-1}. This range is appropriate given the limited strain in the porphyroclasts at the shear zone boundaries (section 4.5.3).

The contrast in rheology between gabbro and plagioclase in the dislocation creep regime is well explained by strengthening due to the presence of hard inclusions (i.e., pyroxenes). Both experimental and theoretical studies indicate that the addition of pyroxene increases the strength of gabbroic rocks in the dislocation creep regime. For example, experimental studies on natural diabase (a fine-grained rock with gabbroic composition) demonstrate that samples with ~70 vol% plagioclase are significantly weaker than those with 56 vol% plagioclase [*Mackwell et al*., 1998]. The contrast in rheology of the plagioclase layers and the coarse gabbros is also consistent with the experimental study of *Dimanov and Dresen* [2005] and the theoretical mixing relationships reviewed by *Tullis et al*. [1991] and *Dimanov and Dresen* [2005]. The effect of plagioclase content is illustrated in Figure 13a, where the diabase with 70% plagioclase is predicted to deform at a strain rate equivalent to that of anorthite, while

diabase with 56% plagioclase is predicted to deform at the same strain rate as coarse gabbro. The difference in strain rate of the two diabases is similar at 925 ºC (Figure 13b), but the strain rates are lower relative to the anorthite and gabbro. One consequence of the pyroxene-hardening effect is that modal variations within gabbro can promote strain localization within plagioclase rich layers [see also *Olgaard*, 1990].

In summary, the experimental flow laws provide accurate estimates for stress and strain rate during dislocation creep of plagioclase and coarse-grained gabbro, but the strain rate for diffusion creep of fine-grained gabbro may be underestimated, particularly at low stresses. The deformation mechanisms predicted by anorthite flow laws and gabbro flow laws are in good agreement with the dominant mechanisms determined by microstructural observations. Our results indicate that diffusion creep in gabbro mylonite layers is promoted by second phase pinning and an inhibition of dislocation creep by the presence of pyroxene, which acts as a hard inclusion.

5.3. Enhanced diffusion creep in fine-grained polyphase materials

In this section we introduce two speculative solutions to the discrepancy between our results and the experimental diffusion creep laws for polyphase material. First, we consider whether relatively rapid interphase diffusion (interphase boundary as opposed to grain boundary) could enhance diffusion creep. Second, we analyze the possibility that the grain size dependence for diffusion creep is not as great as assumed in the flow laws.

Diffusion creep may be enhanced in polyphase materials if interphase boundary diffusion is faster than grain boundary diffusion [e.g., *Bruhn et al*., 1999; but see also *Barnhoorn et al*., 2005]. This effect may not be evident in the experimental studies owing to the microstructure produced during the hot-pressing stage, in which relatively large pyroxene grains (~35 μm) are dispersed within a much finer-grained (~3.5 μm) plagioclase matrix [see Fig. 1d of *Dimanov and Dresen*, 2005]. By contrast, pyroxene and plagioclase are intimately mixed in the SWIR samples and the grain size of the pyroxene is 20 to 60% smaller than the plagioclase (Figure 3b). Thus, there is a significantly higher fraction of interphase boundaries in the natural samples. For

example, assuming an assemblage of cubic grains for simplicity, the ratio of interphase boundaries to grain boundaries in the synthetic sample is approximately 1:10. By contrast, the microstructures of the natural samples exhibit approximately a 1:1 ratio. For both textures nearly all boundaries involving pyroxene are interphase boundaries. To account for the difference in strain rate illustrated in Figure 13b, an "interphase boundary diffusion" effect would require an enhancement in creep rate of approximately a factor of 10 at 925 ºC.

Another way to increase the rate of diffusion creep is to decrease grain size dependence. The grain size exponent (p) for the polyphase flow laws is not well quantified. The discrepancy between the flow law and our microstructural constraints is greatest at large grain size (Figure 12), where the extrapolation in grain size from the lab conditions is greatest. As shown in Figure 13, all four of our microstructural criteria summarized in section 5.2.2 are met by decreasing p from 3 to 2.4 in the diffusion creep flow law for gabbro. A decrease in grain size exponent may arise owing to a transition from grain boundary diffusion limited creep (i.e., Coble creep, $p = 3$) to volume diffusion limited creep (i.e., Nabarro-Herring creep, $p = 2$) with increasing grain size.

5.4. Implications for strength of lower crust

To evaluate the weakening effect that strain localization has on gabbroic crust, we compare the calculated strain rates for SWIR gabbros with and without shear zones. Our analyses suggest that the strain rate in the shear zones is in the range of 10^{-12} s^{-1} to 10^{-11} s^{-1}, while the strain rate outside of the shear zones is in the range of 10^{-14} s^{-1} to 10^{-13} s^{-1} (Figure 13). We model the bulk strain rate of a crust with shear zones using the relationship: $\dot{\varepsilon}_{bulk} = \dot{\varepsilon}_{sz}\chi + \dot{\varepsilon}_{cr}(1-\chi)$, where $\dot{\varepsilon}_{bulk}$ is the bulk crustal strain rate, $\dot{\varepsilon}_{sz}$ is the strain rate in the shear zone, $\dot{\varepsilon}_{cr}$ is the strain rate in the country rock and χ is the fraction of shear zones. Using the 50An/50Cpx flow law from *Dimanov and Dresen* [2005], and assigning $\chi = 0.1$ (i.e., 10% of the crust is mylonite, as observed in the SWIR drill core), $d_{gabbro\ mylonite} = 35$ μm, and $d_{coarse\ gabbro} = 3000$ μm, the bulk strain rate is approximately a factor of two faster in gabbro with shear zones than in gabbro without shear zones at a

stress of 50 MPa (Figure 14). If we modify the grain exponent to $p = 2.4$, as discussed in section 5.3, strain rate in the crust with shear zones increases by another factor of 2. From Figure 14 it is evident that the reduction in the bulk effective viscosity is much smaller than the contrast in effective viscosity between the shear zone and the country rock. Such distinctions could be important for interpreting the distribution of post-seismic strain in the lower crust. Figure 14 also shows that in the absence of shear zones there would be little contrast in the rheology of the crust and mantle below the oceanic crust, or in other tectonic environments where the gabbroic crust is dry, such as below parts of Tibet [*Hacker et al*., 2000] or Venus [*Mackwell et al*., 1998].

6. Conclusions

Microstructural analyses of deformed gabbro mylonites suggest that the extrapolation of experimental flow laws to geologic strain rates is robust. The agreement between predicted and observed deformation mechanisms is best for fine-grained plagioclase mylonite layers and coarse-grained gabbro. The concurrent activity of dislocation creep in the plagioclase mylonite layers and diffusion creep in gabbro mylonite layers is consistent with theoretical and experimental studies on the rheological effects of hard inclusions (i.e., pyroxene) in a weaker matrix. Our analysis suggests that the flow law for diffusion creep of fine-grained gabbro underestimates strain rate by a factor of five to ten. We speculate that diffusion creep may be enhanced due to the higher percentage of interphase boundaries in the natural mylonites compared to the synthetic aggregates of *Dimanov and Dresen* [2005]. Alternatively, the grain size exponent may be smaller than assumed in the experimental flow laws.

Recrystallized plagioclase in monophase layers exhibit strong LPOs. Subgrain boundaries within porphyroclasts appear to be composed of tiltwalls due to slip on (010)[001], while the recrystallized layers have LPOs consistent with slip on (010)[100] and/or (001)[100]. These observations indicate that either the dominant slip systems that characterize the LPO depend on more than just the critical resolved shear stress for each

slip system, or that subgrain boundaries in plagioclase porphyroclasts are not dominantly composed of dislocations from the easiest slip systems.

Polyphase layers originate at clinopyroxene porphyroclasts and are progressively mixed with distance from the host. Fine-grained pyroxene forms by a combination of dynamic recrystallization and orthopyroxene-clinopyroxene exsolution. The plagioclase grain size in mixed layers is smaller than in neighboring monophase plagioclase layers and is well modeled with the Zener pinning relationships. Plagioclase exhibits a weak LPO or random fabrics in the polyphase layers. Together these observations indicate that pinning and phase mixing promote a transition from dislocation creep to diffusion accommodated grain boundary sliding.

Our analyses indicate that the strain rate of shear zones is one to two orders of magnitude greater than the strain rate of gabbroic rock outside of the shear zones. The difference in viscosity is primarily a result of the grain size sensitivity to deformation of the fine-grained gabbro. However, variations in the modal abundance of plagioclase can also promote viscosity contrasts that are exploited to promote strain localization. For a crust with 10% shear zones, as identified for the SWIR gabbros, strain localization decreases the bulk viscosity by a factor of 2 to 4 relative to that of gabbroic crust without shear zones. This limited weakening effect implies that the gabbroic crust has a viscosity similar to the underlying dry mantle for the deformation conditions estimated from the SWIR shear zones.

Acknowledgements

I thank Louis Kerr and Scott Sitzman for EBSD assistance, Neel Chatterjee and Tim Grove for microprobe assistance, and Nick Austin, Henry Dick, Brian Evans, Greg Hirth, Bobbie John, Brian deMartin, David Prior, Marshall Sundberg, and Jessica Warren for discussions throughout the project. I am also grateful for the helpful reviews provided by David Prior, Steven Mackwell and Janelle Homburg. This work was supported with NSF Grants EAR-0230267 and EAR-0409609.

References

Andersen, D. J., D. H. Lindsley, and P. M. Davidson (1993), QUILF; a Pascal program to assess equilibria among Fe-Mg-Mn-Ti oxides, pyroxenes, olivine, and quartz, *Comput. Geosci.*, *19,* 1333-1350.

Ashby, M. F., and R. A. Verrall (1973), Diffusion-accommodated flow and superplastic creep, *Acta Metall., 21,* 149-163.

Austin, N. J., and B. Evans (2007), Paleowattmeters: A scaling relation for dynamically recrystallized grain size, *Geology*, *35*, 343-346.

Baines, A. G., M. J. Cheadle, H. J. B. Dick, A. Hosford Scheirer, B. E. John, N. J. Krusznir, and T. Matsumoto, (2003), Mechanism for generating the anomalous uplift of oceanic core complexes: Atlantis Bank, southwest Indian Ridge, *Geology, 31,* 1105-1108.

Barnhoorn, A., M. Bystricky, K. Kunze, L. Burlini, and J-P. Burg (2005), Strain localization in bimieralic rocks: Experimental deformation of synthetic calcite-anhydrite aggregates, *Earth Planet. Sci. Lett.*, *240*, 748-763.

Bestmann, M., and D. J. Prior (2003), Intragranular dynamic recrystallization in naturally deformed calcite marble: diffusion accommodated grain boundary sliding as a result of subgrain rotation recrystallization, *J. Struct. Geol., 25,* 1597-1613.

Bestmann, M., D. J. Prior, and B. Grasemann (2006), Characterisation of deformation and flow mechanics around porphyroclasts in a calcite marble ultramylonite by means of EBSD analysis, *Tectonophysics, 413,* 185-200.

Bloomer, S.H., P. S. Meyer, H. J. B. Dick, K. Ozawa, and J. H. Natland (1991), Texture and mineralogic variations in grabbroic rocks from Hole 735B, in *Proceedings of the Ocean Drilling Program Scientific Results*, *118,* edited by R. P. Von Herzen et al., *pp.* 21-39, Ocean Drill. Program, College Station, Tex.

Boullier, A. M., and Y. Gueguen (1975), SP-Mylonites: Origin of some mylonites by superplastic flow, *Contrib. Mineral. Petrol., 50*, 93-104.

Brown, J. W., and R. S. White (1994), Variation with spreading rate of oceanic crustal thickness and geochemistry, *Earth Planet. Sci. Lett.*, *121*, 435-449.

Bruhn, D. F., D. L. Olgaard, and L. N. Dell'Angelo (1999), Evidence for enhanced deformation in two-phase rocks: Experiments on the rheology of calcite-anhydrite aggregates, *J. Geophys. Res., 104,* 707-724.

Byerlee, J. D. (1978), Friction of rocks, *Pure Appl. Geophys., 116,* 615-626.

Cannat, M. (1991), Plastic Deformation at an Oceanic Spreading Ridge: A Microstructural Study of the Site 735 gabbros (Southwest Indian Ocean), in *Proceedings of the Ocean Drilling Program Scientific Results*, *118,* edited by R. P. Von Herzen et al., *pp.* 399-408, Ocean Drill. Program, College Station, Tex.

de Bresser, J. H. P., J. H. Ter Heege, and C. J. Spiers (2001), Grain size reductions by dynamic recrystallization: can it result in major rheological weakening?, *Int. J. Earth Sciences (Geol Rundsch), 90,* 28-45.

Dick, H. J. B., H. Schouten, P. S. Meyer, D. G. Gallo, H. Bergh, R. Tyce, P. Patrriat, K. T. M. Johnson, J. Snow, and A. T. Fisher (1991), Tectonic evolution of the Atlantis II Fracture Zone, in *Proceedings of the Ocean Drilling Program Scientific Results*, *118,* edited by R. P. Von Herzen, and P. T. Robinson, *pp.* 359-398, Ocean Drill. Program, College Station, Tex.

Dick, H. J. B., et al. (1999), Leg 176 Summary, in *Proceedings of the Ocean Drilling Program, Initial Reports*, *176* [CD-ROM], edited by J. A. Marin, 70 pp., Ocean Drill. Program, College Station, Tex.

Dick, H. J. B., et al. (2000), A long in situ section of the lower ocean crust: results of ODP Leg 176 drilling at the Southwest Indian Ridge, *Earth Planet. Sci. Lett., 179,* 31-51.

Dick, H. J. B., J. Lin, and H. Schouten (2003), An ultraslow-spreading class of ocean ridge, *Nature*, *426*, 405-412.

Dimanov, A., and G. Dresen (2005), Rheology of synthetic anorthite-diopside aggregates: Implications for ductile shear zones, *J. Geophys. Res., 110,* B07203.

Fliervoet, T. F., S. H. White, and M. R. Drury (1997), Evidence for dominant grain-boundary sliding deformation in greenschist- and amphibolite-grade polymineralic ultramylonites from the Redbank Deformed Zone, Central Australia, *J. Struct. Geol., 19,* 1495-1520.

Fliervoet, T. F., M. R. Drury, P. N. Chopra (1999), Crystallographic preferred orientations and misorientations in some olivine rocks deformed by diffusion and dislocation creep, *Tectonophysics*, *303*, 1-27.

Francis, T. J. G., and R. W. Raitt (1967), Seismic refraction measurements in the southern Indian Ocean, *J. Geophys. Res.*, *72*, 3015-3041.

Freed, A. M. and R. Burgmann (2004), Evidence of powerlaw flow in the Mojave Desert mantle, *Nature, 430*, 548-551.

Hacker, B. R., E. Gnos, L. Ratschbacher, M. Grove, M. O. McWilliams, S. V. Sobolev, J. Wan, and Z. Wu (2000), Hot and dry deep crustal xenoliths from Tibet, *Science*, *287*, 2463-2466.

Halfpenny, A., D. J. Prior, and J. Wheeler (2006), Analysis of dynamic recrystallization and nucleation in a quartzite mylonite, *Tectonophysics, 427,* 3-14.

Handy, M. R. (1990), The solid-state flow of polymineralic rocks, *J. Geophys. Res., 95,* 8647-8661.

Haroun, N. A., and D. W. Budworth (1968), Modifications to the Zener formula for limitation of grain size, *J. Mat. Sci., 3,* 326-328.

Heidelbach, F., A. Post, and J. Tullis (2000), Crystallographic preferred orientation in albite samples deformed experimentally by dislocation and solution precipitation creep, *J. Struct. Geol., 22,* 1649-1661.

Hellman, P., and M. Hillert (1975), On the effect of second-phase particles on grain growth, *Scand. J. Metall., 4,* 211-219.

Hirth, G., J. Escartín, and J. Lin (1998), The rheology of the lower oceanic crust: Implications for lithospheric deformation at mid-ocean ridges, *Geophys. Monograph, 106,* 291-303.

Hobbs, B. E. (1968), Recrystallization of single crystals of quartz, *Tectonophysics*, *6*, 353-401.

Jackson, J. (2002), Strength of the continental lithosphere: Time to abandon the jelly sandwich?, *GSA Today*, *12*, 4-10.

Jaeger, J. C., and N. W. G. Cook (1969), *Fundamentals of Rock Mechanics*, 513 pp., Methuen and Co., LTD, London.

Ji, S., and D. Mainprice (1988), Natural deformation fabrics of plagioclase: implications for slip systems and seismic anisotropy, *Tectonophysics, 147*, 145-163.

Ji, S., D. Mainprice, and F. Boudier (1988), Sense of shear in high-temperature movement from the fabric asymmetry of plagioclase feldspars, *J. Struct. Geol., 10,* 73-81.

Ji, S., R. Wirth, E. Rybacki, and Z. Jiang (2000), High-temperature plastic deformation of quartz-plagioclase multilayers by layer-normal compression, *J. Geophys. Res., 105,* 16651-16664.

Ji, S., Z. Jiang, E. Rybacki, R. Wirth, D. Prior, and B. Xia (2004), Strain softening and microstructural evolution of anorthite aggregates and quartz-anorthite layered composites deformed in torsion, *Earth Planet. Sci. Lett., 222,* 377-390.

Jiang, Z., D. J. Prior, and J. Wheeler (2000), Albite crystallographic preferred orientation and grain misorientation distribution in a low-grade mylonite: implications for granular flow, *J. Struct. Geol., 22,* 1663-1674.

John, B. E., D. A. Foster, J. M. Murphy, M. J. Cheadle, A. G. Baines, C. M. Fanning, and P. Copeland (2004), Determining the cooling history of in situ lower oceanic crust—Atlantis Bank, SW Indian Ridge, *Earth Planet. Sci. Lett., 222,* 145-160.

Karato, S-I., M. Toriumi, and T. Fujii (1980), Dynamic recrystallization of olivine single crystals during high-temperature creep, *Geophys. Res. Lett., 7,* 649-652.

Kohlstedt, D. L., B. Evans, and S. J. Mackwell (1995), Strength of the lithosphere: Constraints imposed by laboratory experiments, *J. Geophys. Res., 100,* 17587-17602.

Kruse, R., and H. Stünitz (1999), Deformation mechanisms and phase distribution in mafic high-temperature mylonites from the Jotun Nappe, southern Norway, *Tectonophysics*, *303*, 223-249.

Kruse, R., H. Stünitz, and K. Kunze (2001), Dynamic recrystallization processes in plagioclase porphyroclasts, *J. Struct. Geol., 23,* 1781-1802.

Lapworth, T., J. Wheeler, and D. J. Prior (2002), The deformation of plagioclase investigated using electron backscatter diffraction crystallographic preferred orientation data, *J. Struct. Geol., 24,* 387-399.

Lindsley, D. H., and B. R. Frost (1992), Equilibria among Fe-Ti oxides, pyroxenes, olivine, and quartz: Part I. Theory, *Am. Mineral., 77*, 987-1003.

Lloyd, G. E., A. B. Farmer, and D. Mainprice (1997), Misorientation analysis and the formation and orientation of subgrain and grain boundaries, *Tectonophysics*, *279*, 55-78.

Mackwell, S. J., B. E. Zimmerman, and D. L. Kohlstedt (1998), High-temperature deformation of dry diabase with application to tectonics on Venus, *J. Geophys. Res., 103,* 975-984.

Manning, C. E., P. Weston, and K. I. Mahon (1996), Rapid high-temperature metamorphism of East Pacific Rise gabbros from Hess Deep, *Earth Planet. Sci. Lett.*, *144*, 123-132.

Marshall, D. B., and A. C. McLaren (1977), Deformation mechanisms in experimentally deformed plagioclase feldspars, *Phys. Chem. Minerals, 1,* 351-370.

Miranda, E. A. (2006), Structural development of the Atlantic Bank oceanic detachment fault system, Southwest Indian Ridge, *Ph.D. Thesis*, University of Wyoming, Laramie, Wyoming.

Montesi, L. G. J., and G. Hirth (2003), Grain size evolution and rheology of ductile shear zones: from laboratory experiments to postseismic creep, *Earth Planet. Sci. Lett., 211,* 97-110.

Muller, M. R., C. J. Robinson, T. A. Minshull, R. S. White, and M. J. Bickle (1997), Thin crust beneath the Ocean Drilling Program Borehole 735B at the Southwest Indian Ridge?, *Earth Planet. Sci. Lett., 148,* 93-107.

Newman, J., A. K. Kronenberg, and W. M. Lamb (1994), Strength of oceanic crust, *Eos. Trans. AGU, Spring Meet. Suppl*., *75,* 229.

Newman, J., W. M. Lamb, M. R. Drury, R. L. M. Vissers (1999), Deformation processes in a peridotite shear zone: reaction softening by an H_2O-deficient, continuous net transfer reaction, *Tectonophysics*, 303, 193-222.

Nicolas, A., and J. P. Poirier (1976), *Crystalline Plasticity and Solid State Flow in Metamorphic Rocks*, 444 pp., John Wiley, Hoboken, N. J.

Nye, J.F. (1953), The flow law of ice from measurements in glacier tunnels, laboratory experiments and the Jungfraufirn borehole experiment, *Proc. Roy. Soc. London, Ser. A, 219*, 477-489.

Offerhaus, L. J., R. Wirth, and G. Dresen (2001), High-temperature creep of polycrystalline albite, in *Deformation Mechanisms, Rheology and Tectonics*, edited by S. de Meer, et al., 124 pp., Utrecht Univ., Noordwijkerhout, The Netherlands.

Olesen, N. Ø., (1987) Plagioclase fabric development in a high-grade shear zone, Jotunheimen, Norway, *Tectonophysics, 142,* 291-308.

Olsen, T. S., and D. L. Kohlstedt (1985), Natural deformation and recrystallization of some intermediate plagioclase feldspars, *Tectonophysics, 111,* 107-131.

Olgaard, D. L., and B. Evans (1986), Effect of Second-Phase Particles on Grain Growth in Calcite, *J. Am. Ceram. Soc., 69*, 272-277.

Olgaard, D. L. (1990), The role of second phase in localizing deformation, in *Deformation Mechanisms, Rheology and Tectonics, 54,* edited by R. J. Knipe, and E. H. Rutter, 175-181*,* Geological Society of London, London.

Post, A., and J. Tullis (1999), A recrystallized grain size piezometer for experimentally deformed feldspar aggregates, *Tectonophysics, 303,* 159-173.

Prior, D. J. (1999), Problems in determining the misorientation axes, for small angular misorientations, using electron backscatter diffraction in the SEM, *J. Microsc*, *24*, 999-1011.

Prior, D. J., and J. Wheeler (1999), Feldspar fabrics in a greenschist facies albite-rich mylonite from electron backscatter diffraction, *Tectonophysics, 303,* 29-49.

Raj, R., and M. F. Ashby (1971), On grain boundary sliding and diffusional creep, *Metall. Trans., 2,* 1113-1127.

Ramsay, J.G. (1980), Shear zone geometry: a review, *J. Struct. Geol., 2,* 83-99.

Rutter, E. (1999), On the relationship between the formation of shear zones and the form of the flow law of rocks undergoing dynamic recrystallization, *Tectonophysics*, *303*, 147-158.

Rybacki, E., and G. Dresen (2000), Dislocation and diffusion creep of synthetic anorthite aggregates, *J. Geophys. Res., 105,* 26017-26036.

Rybacki, E., and G. Dresen (2004), Deformation mechanism maps for feldspar rocks, *Tectonophysics, 382,* 173-187.

Rybacki, E., M. Gottschalk, R. Wirth, and G. Dresen (2006), Influence of water fugacity and activation volume on flow properties of fine-grained anorthite aggregates, *J. Geophys. Res., 111,* B03203, doi: 10.1029/2005JB003663.

Schmid, S. M., J. N. Boland, and M. S. Paterson (1977), Superplastic flow in finegrained limestone, *Tectonophysics, 43,* 257-291.

Schmid, S. M., R. Panozzo, and S. Bauer (1987), Simple shear experiments on calcite rocks; rheology and microfabric, *J. Struct. Geol., 9,* 747-778.

Siegesmund, S, K. Helming, and R. Kruse (1994), Complete texture analysis of a deformed amphibolite: comparison between neutron diffraction and U-stage data, *J. Struct. Geol., 16,* 131-142.

Skemer, P., I. Katayama, Z. Jiang, and S-I. Karato (2005), The misorientation index, Development of a new method for calculating the strength of lattice-preferred orientation, *Tectonophysics*, *411*, 157-167.

Stünitz, H., J. D. Fitz Gerald, and J. Tullis (2003), Dislocation generation, slip systems, and dynamic recrystallization in experimentally deformed plagioclase single crystals, *Tectonophysics, 372,* 215-233.

Tödheide, K. (1972), Water at high temperatures and pressures, in *Water, a Comprehensive Treatise,* edited by F. Granks, pp. 463-514, Plenum, New York.

Tullis, T., F. G. Horowitz, and J. Tullis (1991), Flow laws of polyphase aggregates from end-member flow, *J. Geophys. Res., 96,* 8081-8096.

Twiss, R. T. (1977), Theory and Applicability of a Recrystallized Grain Size Paleopiezometer, *Pure Appl. Geophys., 115,* 227-244.

Underwood, E. E. (1970), *Quantitative Stereology*, 274 pp., Addison- Wesley-Longman, Reading, Mass.

Urai, J. L., W. D. Means, and G. S. Lister (1986), Dynamic recrystallization of minerals, *Geophys. Monograph, 36,* 161-199.

Van der Wal, D., P. Chopra, M. Drury, and J. Fitz Gerald (1993), Relationships between dynamically recrystallized grain size and deformation conditions in experimentally deformed olivine rocks, *Geophys. Res. Lett., 20,* 1479-1482.

Vanko, D. A., and D. S. Stakes (1991), Fluids in oceanic Layer 3: evidence from veined rocks, Hole 735B, Southwest Indian Ridge, in *Proceedings of the Ocean Drilling Program Scientific Results*, *118,* edited by R. P. Von Herzen, and P. T. Robinson, *pp.* 181-215, Ocean Drill. Program, College Station, Tex.

Warren, J.M., and G. Hirth (2006), Grain size sensitive deformation mechanisms in naturally deformed peridotites, *Earth Planet. Sci. Lett., 248,* 423-435.

Wheeler, J., D. J. Prior, Z. Jiang, R. Spiess, and P. W. Trimby (2001), The petrological significance of misorientations between grains, *Contrib. Min. Petrol., 141*, 109-124.

Xie, Y., H-R. Wenk, and S. Matthies (2003), Plagioclase preferred orientation by TOF neutron diffraction and SEM-EBSD, *Tectonophysics, 370,* 269-286.

Yund, R.A., and J. Tullis (1991), Compositional changes of minerals associated with dynamic recrystallization, *Contrib. Mineral. Petrol., 108,* 346-355.

Zimmerman, M., and D. Kohlstedt (2003), Melt segregation and LPO in anorthite-basalt deformed in torsion, *Eos. Trans. AGU, Fall Meet. Suppl*., *84,* Abstract S22E-06.

Table 1 (next page). Microstructure data for SWIR shear zones. Layer labels are provided for comparison with figures. *Description* refers to monophase, polyphase, or oxide (ox-gab) layer or zone. *Phase* is plagioclase, olivine, clinopyroxene, orthopyroxene, ilmenite, or magnetite. When measured, the anorthite content of the plagioclase is listed. *Size* is grain size in μm. *X/Z* is the aspect ratio of recrystallized grains. *%* is the modal percent of the phase. σ is differential stress in MPa. Stresses in italics are estimated based on the stress estimates of neighboring monophase layers. # is the number of grains analyzed by EBSD. *Slip system* lists the most likely slip systems consistent with the LPO. M_i is the M-index, a quantification of the fabric strength.

[a] Layer 155-1C has an anomalously weak fabric. The fabric is stronger for regions of fewer grains within the layer, see Figure A2 in the appendix.

[b] Shear zone layer 188-3.2BA is plotted as a monophase layer in Figure 11 because the clinopyroxene is limited to thin horizons that do not appear to influence grain size.

sample, depth		description	phase	size	X/Z	%	σ	#	slip system	M_i
090-4	C	mono	plag	53	1.0	100	71	200	(010)&(001)[100]	0.11
75.2 m	F	poly ox-gab	plag	39	1.1	15	*104*	200	random	0.04
	F	poly ox-gab	mag/ilm	24	1.1	85				
	H	mono	plag	45	1.2	100	79	200	(001)[100]	0.11
	J	mono	plag			100	79	200	(001)[100]	0.14
	K	mono	plag	30	1.1	100	104	200	(001)[100]	0.10
147-6	A	mono	plag	86	1.1	100	51	200	(010)[100]	0.11
366.6 m	B	poly ox-gab	plag	59	1.3	44	*51*	200	random	0.04
	B	poly ox-gab	cpx	30	1.3	56				
149-3.1A	A	mono	olivine			100		66	rotate to (010)[100]?	
383.2 m	B	poly	An35	54	1.1	66		201	rotate to (001)[100]?	0.07
	B	poly	cpx	78	1.3	34				
	C	poly	plag	57	1.1	46		200		0.06
	C	poly	cpx	45	1.1	54				
149-3.2	A	poly ox-gab	plag	15.8	1.0	77	*61*	227	random	0.04
383.2 m	A	poly ox-gab	mag	6	1.2	18		204	{001}<?>	0.03
	A	poly ox-gab	ilm			5		50	(0001)[?]?	
	B	poly ox-gab	plag	16.2	1.1	87	*61*	202	random	0.05
	B	poly ox-gab	mag/ilm	15	1.0	13				
	C	mono	An38	66	1.2	100	61	200	(010)[100]&[001]?	0.11
155-1	C1	mono	plag	146	1.1	100	36	231	random	0.05[a]
434.5 m	C2	mono	plag			100	*36*	55		
	C3	mono	plag			100	*36*	90		
	D	poly	An50	57	1.3	46	*36*	204	(001)[100]	0.13
	D	poly	cpx	47	1.1	54				
	G	mono	plag			100	*31*	202	inherited	
	K	mono	plag	179	1.0	70	31	200	(010)[100]	0.09
	L	mono	cpx			100		82		
	M	mono	cpx			100		76		
188-3.2A	A	mono	An56	288	1.1	100	22	205	(010)[100]	0.18
711.9 m	B	poly	An57	135	1.2	68	*22*	215	random	0.04
	B	poly	cpx	63	1.5	16		89		
	B	poly	opx			10		53		
	B	poly	olivine			6		34		
	J	mono	plag			100		58		
	K	mono	plag			100		55		
188-3.2B	A[b]	~mono	plag	216	1.1	83	27	201	(001)[100]	0.07
711.9 m	A[b]	~mono	cpx	87	1.2	17		39		
	B	poly	plag	111	1.3	49	*27*	215	random	0.04
	B	poly	cpx	63	1.5	36		83	random	
	B	poly	olivine			15		36	random	
	C	mono	olivine	453	1.1	100	12, 14	100		
	D	mono	cpx			100		71		
	E	mono	plag	314	1.1	100	19			

sample	depth	core	rim
149-3.1	961	933 ± 41	862 ± 60
		946 ± 69	905 ± 60
149-3.2	964	872 ± 57	857 ± 44
		860 ± 70	880 ± 63
155-1	1016	829 ± 23	823 ± 17
		808 ± 14	816 ± 15
188-3.2A	1310	942 ± 36	895 ± 29
		924 ± 34	908 ± 45

Table 2. Recrystallized two-pyroxene temperature estimates for SWIR shear zones. Temperatures are calculated using the Ca-QUILF software of *Lindsley and Frost* [1992]. See Figure 10 for backscattered electron images of the pyroxene breakdown reaction.

Sample	149-3.1				149-3.2				155-1				188-3.2A			
	core	rim	core	rim	core	rim	core	rim	core	rim	core	rim	core	rim	core	rim
SiO_2	52.47	52.38	51.43	52.40	51.83	51.91	52.26	52.51	53.82	53.80	53.23	54.34	51.72	51.85	51.35	51.72
TiO_2	0.49	0.48	0.82	0.48	0.30	0.34	0.25	0.31	0.19	0.32	0.22	0.13	0.74	0.66	0.94	0.76
Al_2O_3	1.71	1.80	2.45	1.96	1.31	1.31	1.44	1.18	1.36	1.84	1.47	1.01	2.70	2.56	2.97	2.78
Cr_2O_3	0.02	0.00	0.00	0.00	0.01	0.00	0.01	0.00	0.01	0.00	0.04	0.02	0.06	0.06	0.07	0.07
FeO	10.73	8.23	9.54	8.83	11.05	10.91	10.60	10.71	7.78	7.80	8.03	6.84	8.00	8.29	7.97	8.19
MnO	0.31	0.25	0.24	0.26	0.44	0.43	0.37	0.38	0.18	0.23	0.25	0.21	0.20	0.23	0.21	0.20
MgO	15.33	14.66	14.58	14.72	13.94	13.97	14.25	14.15	15.09	14.72	14.85	15.22	14.92	15.20	14.55	14.98
CaO	18.89	21.80	20.85	21.47	21.02	20.71	21.09	21.46	22.30	22.06	22.27	22.93	21.24	20.89	21.69	21.79
Na_2O	0.46	0.54	0.50	0.52	0.45	0.49	0.46	0.47	0.39	0.34	0.35	0.23	0.47	0.43	0.57	0.42
Total	100.41	100.13	100.41	100.64	100.37	100.07	100.74	101.17	101.11	101.12	100.70	100.93	100.05	100.17	100.31	100.90

Table 3. Clinopyroxene microprobe analyses

Sample	149-3.1				149-3.2				155-1				188-3.2A			
	core	rim	core	rim	core	rim	core	rim	core	rim	core	rim	core	rim	core	rim
SiO_2	52.90	53.40	53.03	53.48	52.18	52.70	52.70	52.41	54.23	54.30	54.47	54.21	54.13	54.40	53.74	53.93
TiO_2	0.26	0.13	0.34	0.14	0.18	0.09	0.24	0.20	0.18	0.11	0.09	0.06	0.29	0.18	0.32	0.21
Al_2O_3	0.81	0.60	0.93	0.59	0.58	0.42	0.88	0.73	0.84	0.77	0.75	0.70	1.34	1.08	1.36	1.24
Cr_2O_3	0.00	0.00	0.02	0.00	0.01	0.01	0.01	0.02	0.02	0.00	0.01	0.03	0.00	0.00	0.01	0.00
FeO	21.46	21.40	21.05	20.86	24.08	24.08	23.11	23.98	20.25	20.27	19.99	19.97	17.71	16.84	17.61	17.54
MnO	0.54	0.53	0.46	0.48	0.83	0.82	0.83	0.75	0.51	0.36	0.53	0.49	0.40	0.40	0.46	0.38
MgO	22.99	23.41	23.48	23.66	21.31	21.47	21.07	21.33	23.29	23.65	23.83	23.95	25.79	26.52	26.35	26.38
CaO	1.12	0.98	1.29	1.13	0.98	0.92	2.39	1.07	0.83	0.71	0.80	0.77	1.17	0.82	1.00	0.90
Na_2O	0.00	0.00	0.00	0.00	0.04	0.02	0.08	0.03	0.00	0.00	0.00	0.00	0.02	0.00	0.03	0.00
Total	100.08	100.45	100.60	100.34	100.20	100.54	101.30	100.52	100.15	100.18	100.48	100.18	100.85	100.24	100.87	100.59

Table 4. Orthopyroxene microprobe analyses

Sample	155-1		188-3.2A	
	core	rim	core	rim
SiO_2	37.04	37.25	37.35	37.29
TiO_2	0.00	0.00	0.03	0.01
Al_2O_3	0.00	0.00	0.01	0.01
Cr_2O_3	0.00	0.00	0.01	0.00
FeO	31.36	30.73	27.88	28.01
MnO	0.48	0.53	0.37	0.37
MgO	31.32	31.40	34.61	34.41
CaO	0.01	0.01	0.03	0.02
Na_2O	0.02	0.06	0.00	0.01
Total	100.24	99.98	100.28	100.13

Table 5. Olivine microprobe analyses

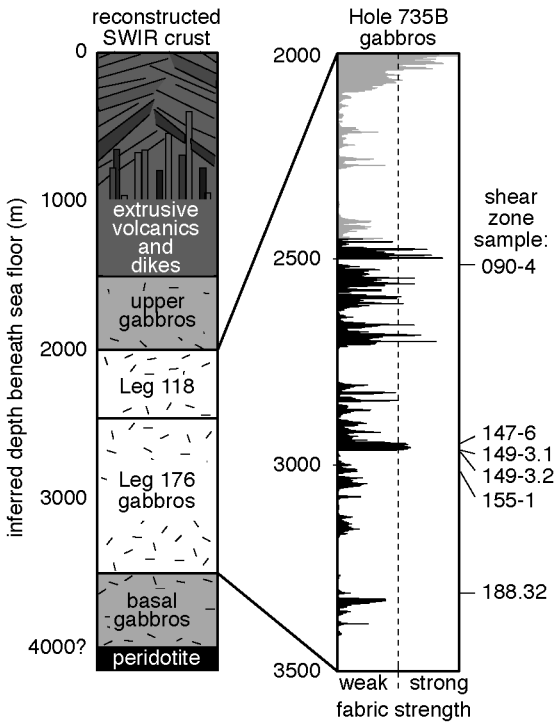

Figure 1. Reconstructed SWIR crustal section. The column on the right shows the running-average crystal plastic fabric strength. We focus on the Leg 176 gabbros. Shear zone sample depths are illustrated at right.

Figure 2 (next page). Photomicrographs of SWIR shear zones. All figures are plane polarized light except (d), which is cross polarized light. Regions pictured in other figures are outlined and labeled. a) Sample 155-1. b) Sample 147-6. c) Sample 188-3.2A. d) Sample 188-3.2A in cross polarized light. Porphyroclasts analyzed in Figure 8 are traced in white. e) Sample 090-4. All photos are in the X-Z reference frame.

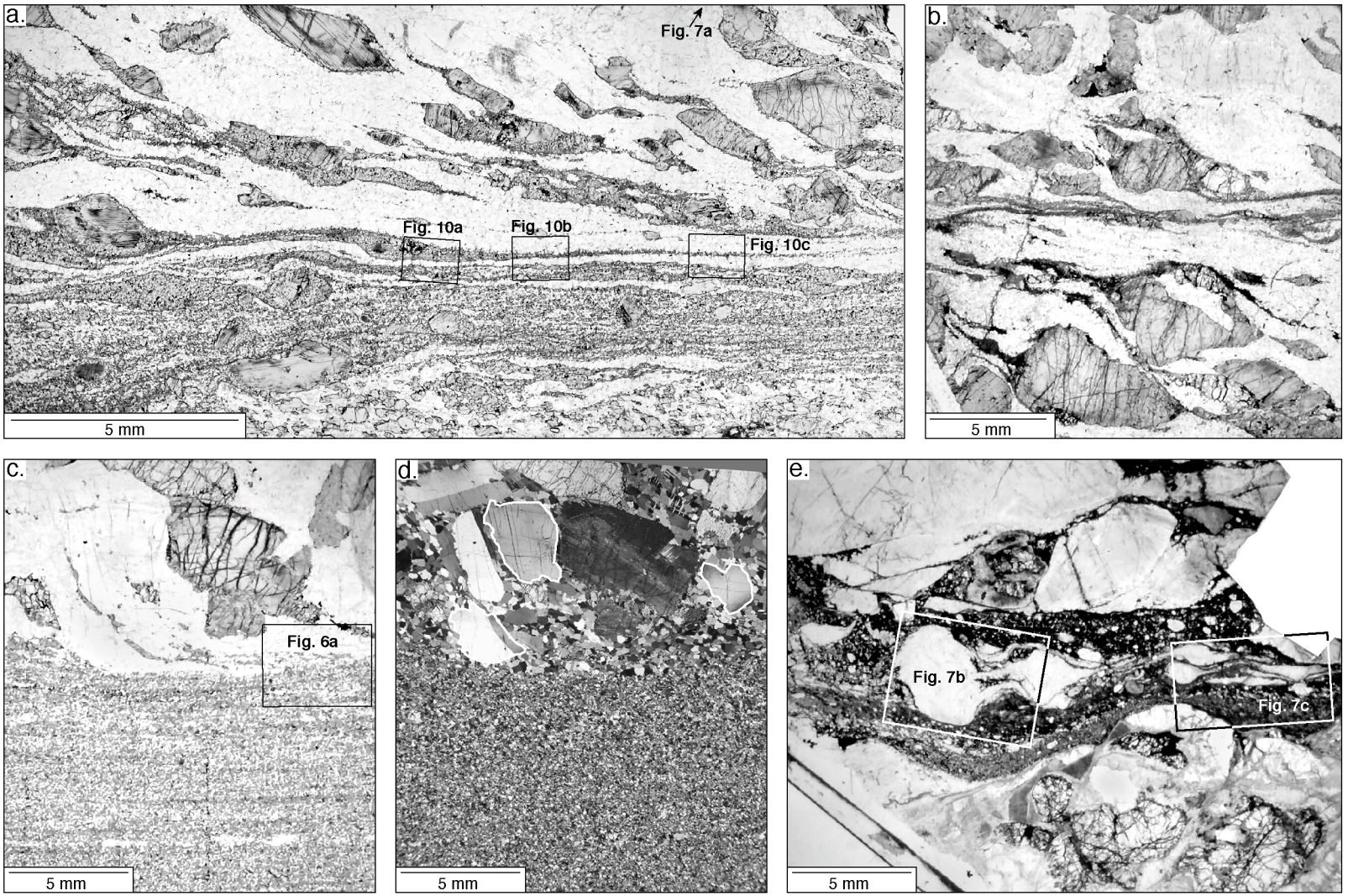
a.
Fig. 7a
Fig. 10a
Fig. 10b
Fig. 10c
5 mm
b.
5 mm
c.
Fig. 6a
5 mm
d.
5 mm
e.
Fig. 7b
Fig. 7c
5 mm

Figure 3 (next page). Cross-polarized photomicrographs of recrystallized plagioclase. a) Nearly monophase recrystallized layer, with plagioclase (plag) and pyroxenes (px) in sample 188-3.2B. Plagioclase commonly exhibits twinning (t). b) Well-mixed gabbro mylonite layer, sample 188-3.2B. Pyroxenes (px) are high relief. c) Recrystallized grains and subgrains (s) in porphyroclasts have similar grain sizes, sample 155-1. d) Recrystallized grain size is smaller than subgrain size in the shear zone with the highest stress estimates, sample 090-4. Note the E-W healed fracture (f) in the porphyroclast.

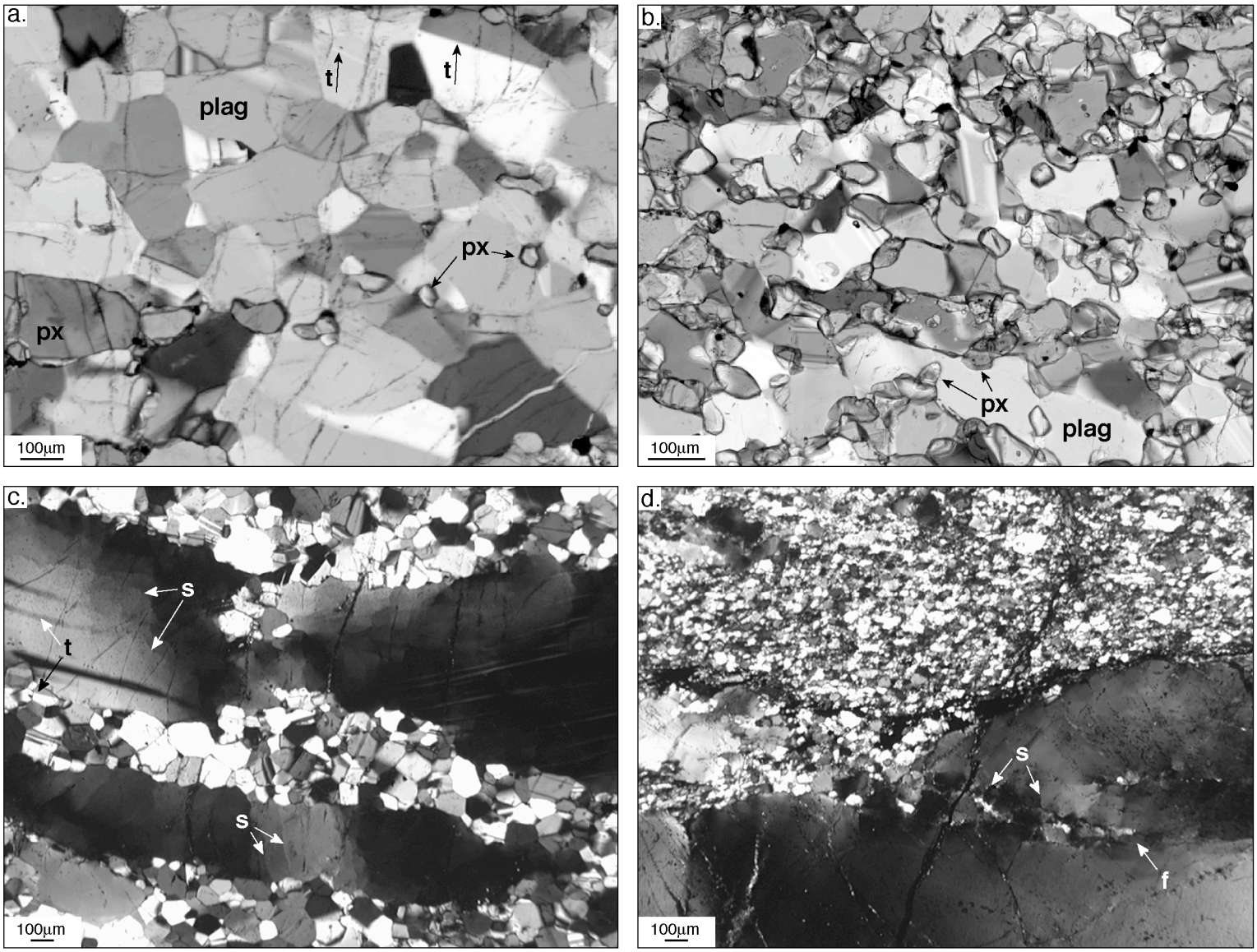
a.
t
t
plag
px
px
100µm
b.
px
plag
100µm
c.
s
t
s
100µm
d.
s
f
100µm

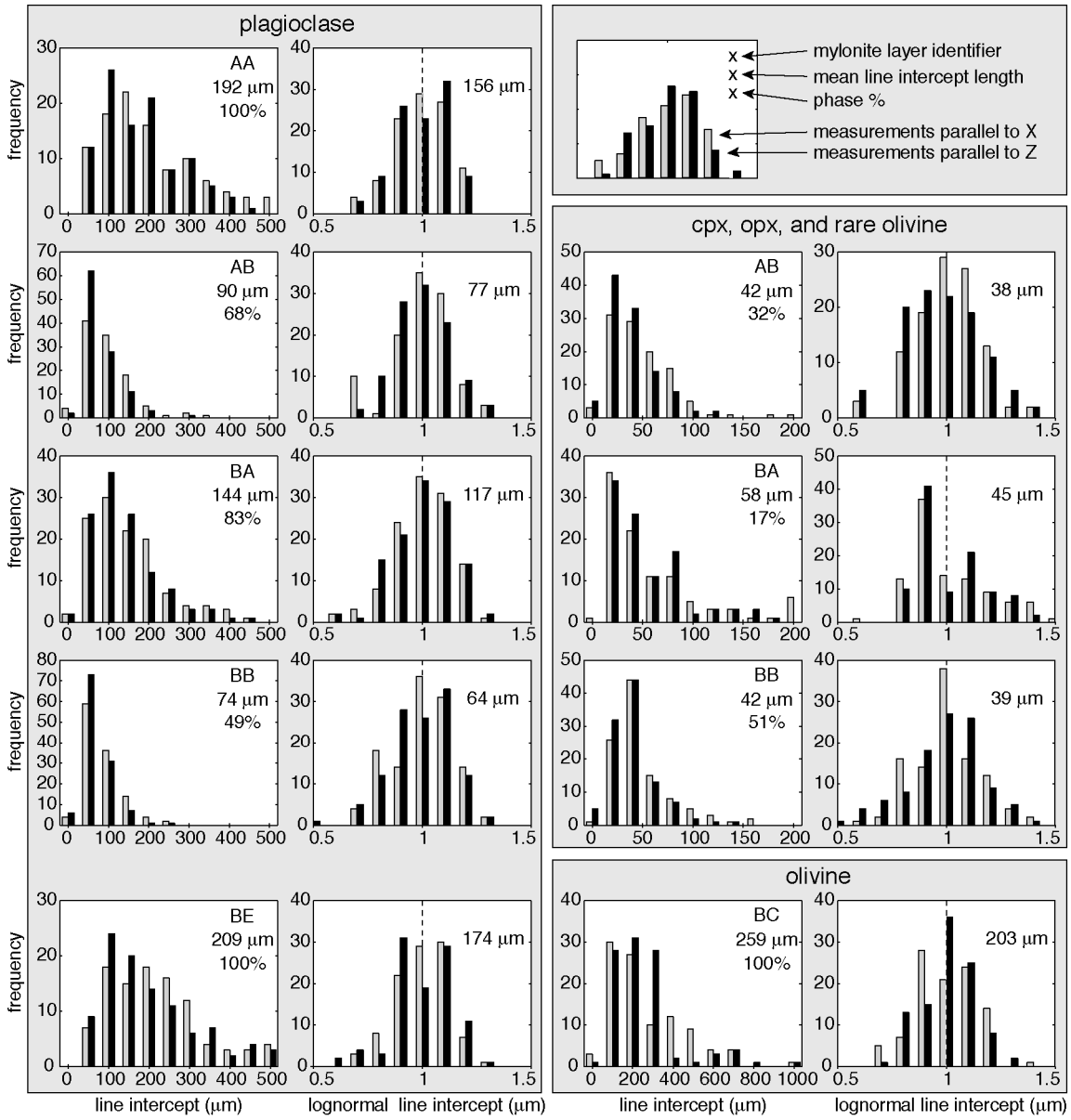

Figure 4. Line-intercept and lognormal length distributions for shear zone 188-3.2. See Figure 6 for texture photomicrographs and Table 1 for microstructure data. Sample label, average grain size and phase proportion are shown in the upper right. Line intercept plots show the arithmetic mean, lognormal plots show the geometric mean. AA and BE are monophase plagioclase layers at the shear zone boundaries. BC is a monophase olivine layer. AB, BA, and BB are polyphase layers.

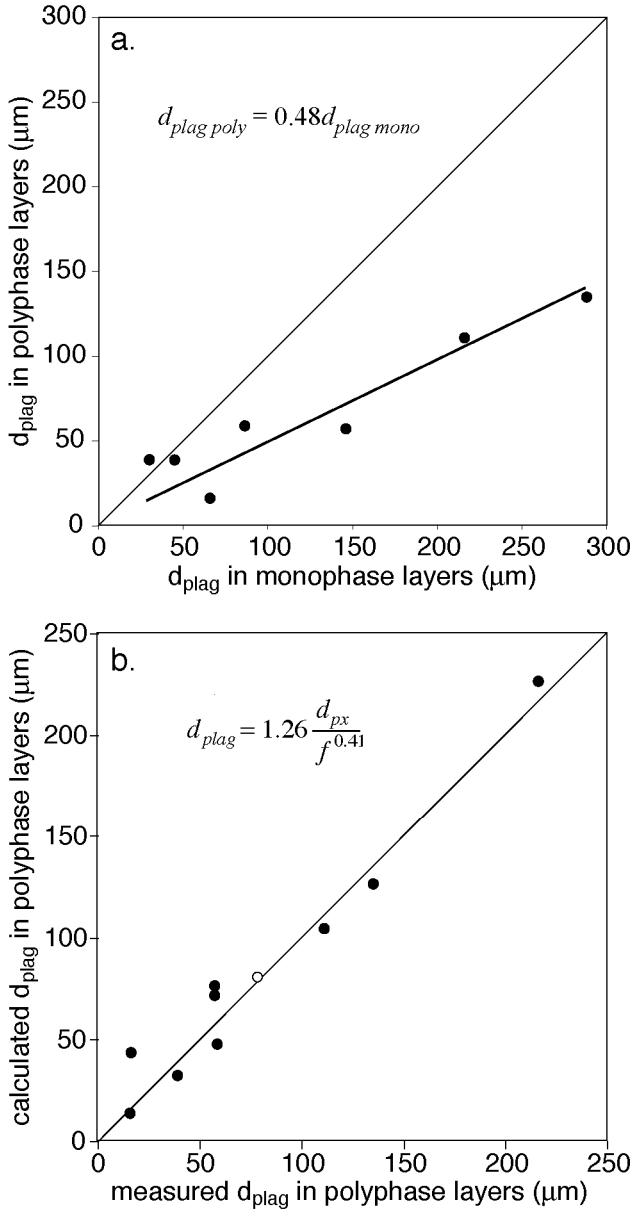

Figure 5. a) Grain size relationship between plagioclase in monophase and gabbro mylonite layers. The best fit line has an R^2 of 0.84. b) Relationship between observed and predicted plagioclase grain size calculated using the Zener pinning relationship. The calculated plagioclase grain size fits a power law derived from a best fit relation for d_{plag} / d_{px} versus pyroxene phase fraction for polyphase shear zone layers, excluding one mylonite layer with $d_{plag} = d_{px}$ ($R^2 = 0.60$). The open symbol denotes a layer with $d_{plag} < d_{px}$ where we treat plagioclase as the pinning phase. The data fits the 1:1 trend line with $R^2 = 0.95$.

Figure 6 (next page). Plane and cross (XPL) polarized photomicrographs and plagioclase (plag), clinopyroxene (cpx), and olivine pole figures for shear zone 188-3.2. Pole figures are generated from the layers separated by white lines in the XPL photomicrographs. Layers are labeled for comparison with Figure 4 and Table 1. Pole figures are lower hemisphere equal area stereonets with the shear plane indicated by the E-W line and lineation at the intersection of the shear plane and the primitive, see the key below the pole figures. *n* is number of grains, *M* is fabric strength for layers with > 200 grains, as calculated with the M-index, and *max* is the maximum density in multiples of m.u.d. The shading grayscale is linear with a maximum at 10 multiples of uniform distribution (m.u.d.). The contour interval is 1σ, the first contour is 2σ. The white circles in (c) indicate the clinopyroxene porphyroclast's location and crystal orientation.

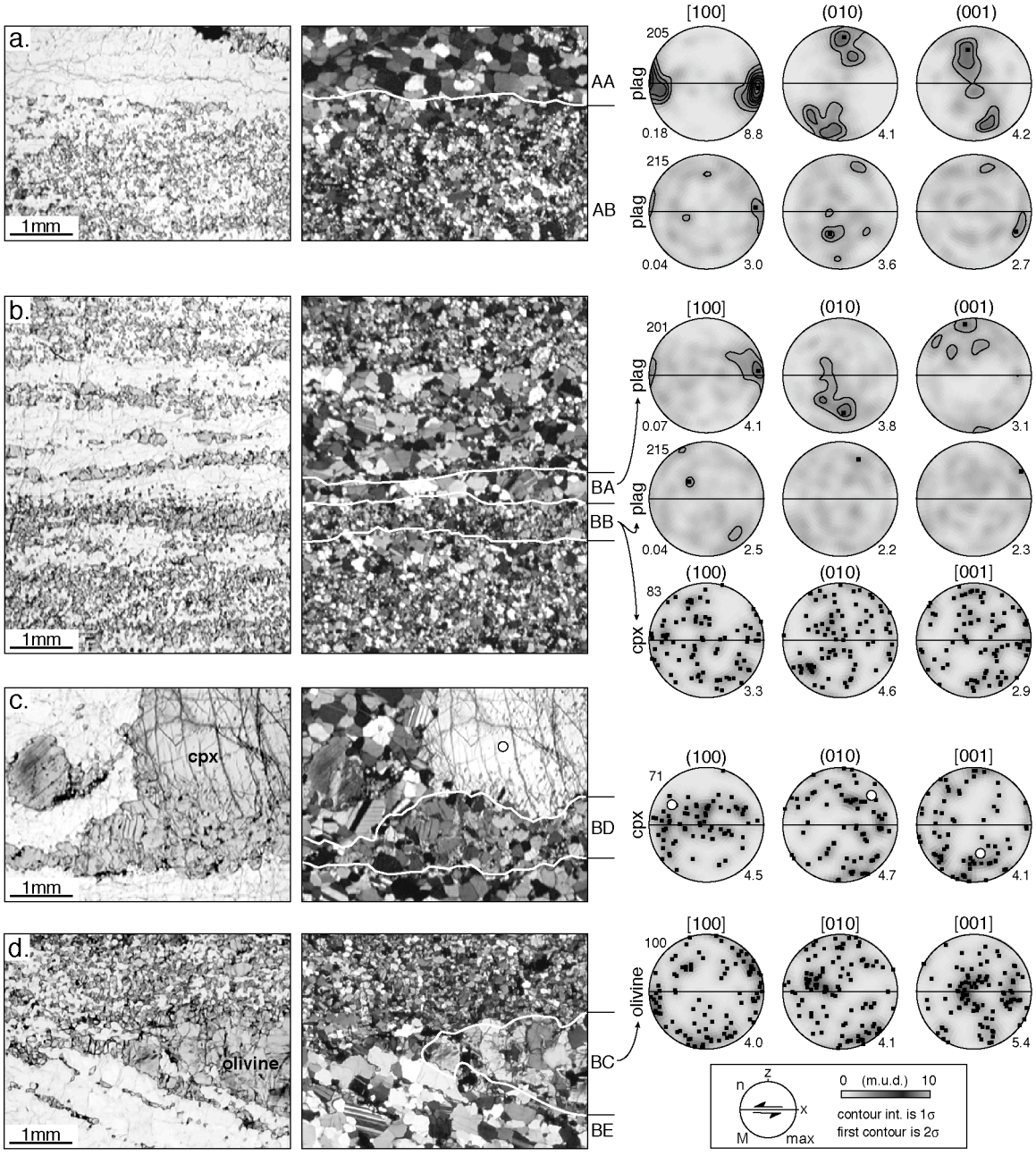
a.
1mm
AA
AB
[100]
(010)
(001)
plag
205
0.18
8.8
4.1
4.2
215
0.04
3.0
3.6
2.7
b.
1mm
BA
BB
201
0.07
4.1
3.8
3.1
215
0.04
2.5
2.2
2.3
(100)
(010)
[001]
cpx
83
3.3
4.6
2.9
c.
cpx
1mm
BD
71
4.5
4.7
4.1
d.
olivine
1mm
BC
BE
100
4.0
4.1
5.4
n
z
x
M
max
0 (m.u.d.) 10
contour int. is 1σ
first contour is 2σ

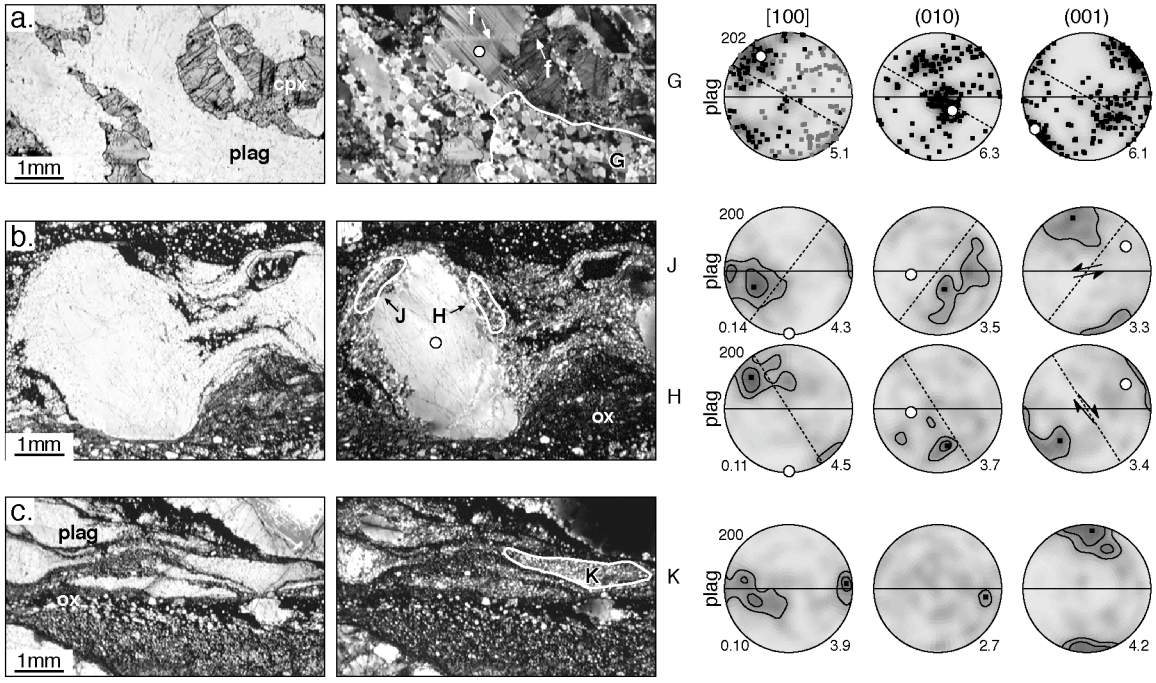

Figure 7. Photomicrographs and lower hemisphere pole figures illustrating different controls on plagioclase slip plane orientation, see Figure 2 for thin section-scale photos and Figure 7 for plotting conventions. a) Host-controlled LPO in sample 155-1. Crystal orientations with the [100] direction intersecting the upper hemisphere are gray. Shading in (a) was generated after projecting the upper hemisphere axes into the lower hemisphere. Note the incipient brittle fracture (f). The local foliation is shown by dashed lines on the pole figures. The white circle identifies the porphyroclast and porphyroclast orientation in the pole figures. cpx = clinopyroxene, plag = plagioclase. b) LPO controlled by a rigid porphyroclast in sample 090-4. The obliquities of [100] with respect to porphyroclast boundaries are consistent with flow around the rigid porphyroclast (black arrows in the pole figures). The shear planes are subparallel to the porphyroclast boundary (dashed lines). ox = Fe-Ti oxides. c) Shear zone boundary-controlled LPO in sample 090-4.

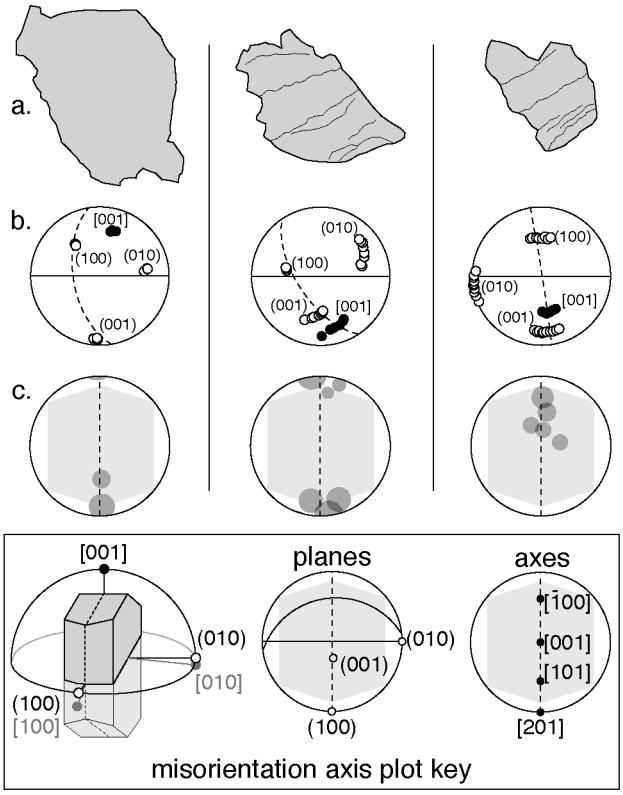

Figure 8. Plagioclase subgrain orientations. a) Porphyroclast outlines with subgrain boundaries. See Figure 2d for location. b) Pole figures, lower hemisphere equal area stereonets. Open symbols indicate poles to planes, solid symbols indicate axes. The average (010) plane is indicated by a dashed line. c) Orientation of subgrain boundary misorientation axes on upper hemisphere equal angle stereonets. 24° and 12° cones represent the errors associated with EBSD analyses for rotations of 3-5° and 5-10° rotations, respectively [Prior, 1999]. The (010) plane is indicated by the dashed line. The key illustrates the crystal reference frame and orientation of plagioclase planes and axes in (b).

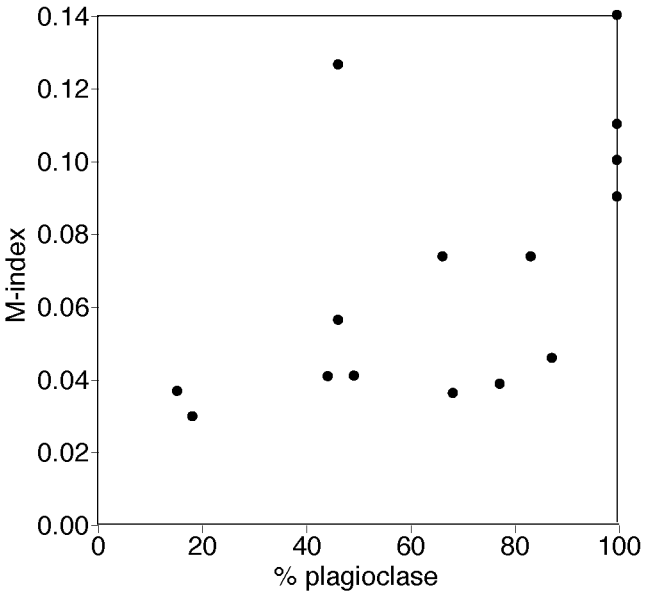

Figure 9. Relationship between fabric strength and modal abundance of plagioclase. Fabric strength is quantified by calculating the M-index [Skemer et al., 2005].

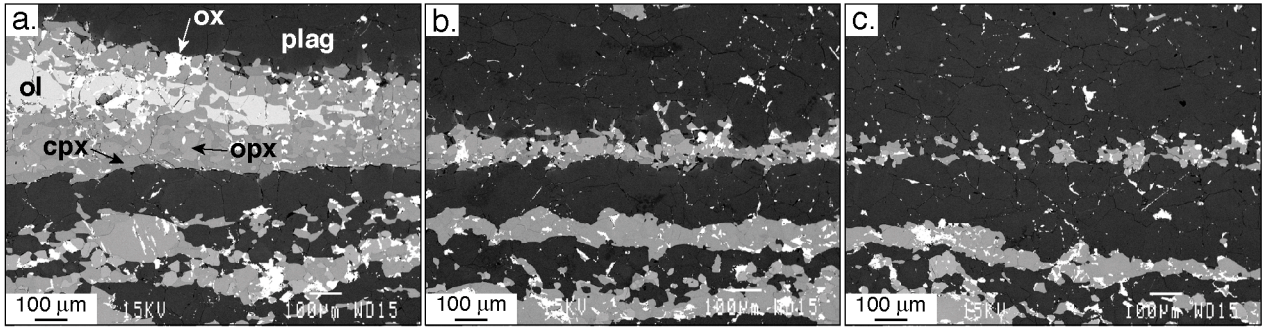

Figure 10. Backscattered electron images showing progressive mixing of pyroxenes from a clinopyroxene porphyroclast (sample 155-1, see Figure 2a for location). Minerals are labeled as: plagioclase (plag), olivine (ol), clinopyroxene (cpx), orthopyroxene (opx), and Fe-Ti oxide (ox).

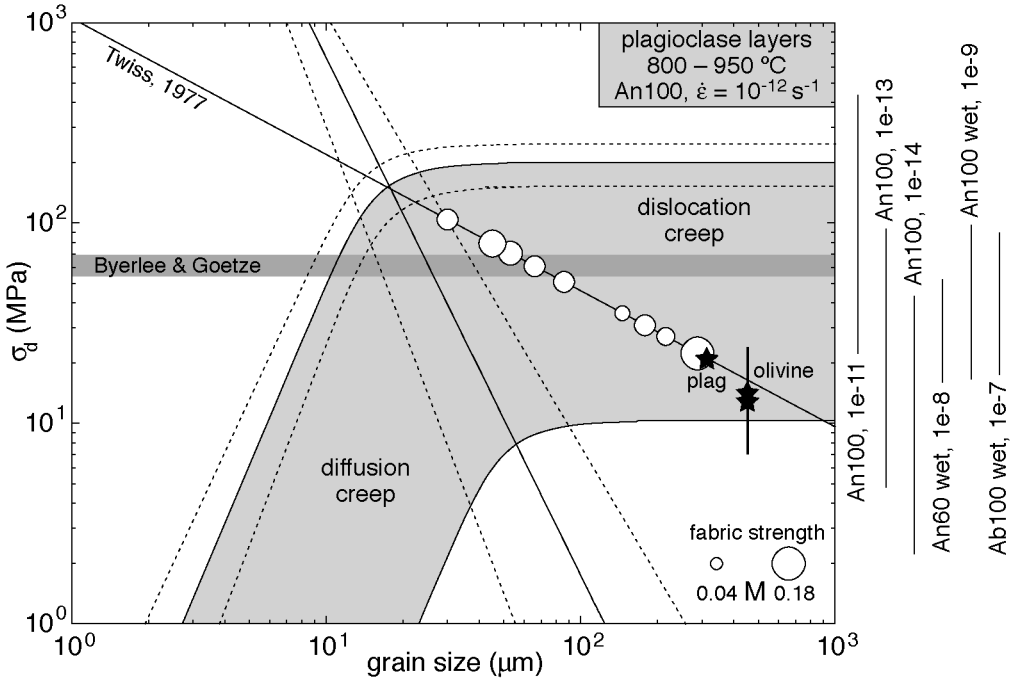

Figure 11. Deformation mechanism map comparing a dry anorthite flow law and SWIR monophase plagioclase mylonite layers. The flow law curves are calculated with parameters from Rybacki and Dresen [2000], at a strain rate of 10^{-12} s^{-1} and at temperatures of 800 and 950 ºC (high and low stress contour, respectively). The dislocation creep stresses for anorthite and wet plagioclase at the same temperature range but different strain rates are shown to the right of the plot, see text for references. Errors associated with Q and n are shown by the dashed lines at the 800 ºC contour and the boundary separating the diffusion and dislocation creep fields. The stresses predicted for frictional sliding (Byerlee) and the brittle-plastic transition (Goetze) for SWIR gabbros are shown by the horizontal gray bar. Monophase mylonite layers are plotted on the Twiss recrystallized grain size piezometer. Symbol size is proportional to fabric strength as quantified with the M-index, see key in the lower right corner. Stars and associated error bar indicate stress estimates for neighboring recrystallized plagioclase and olivine at a shear zone boundary, see text.

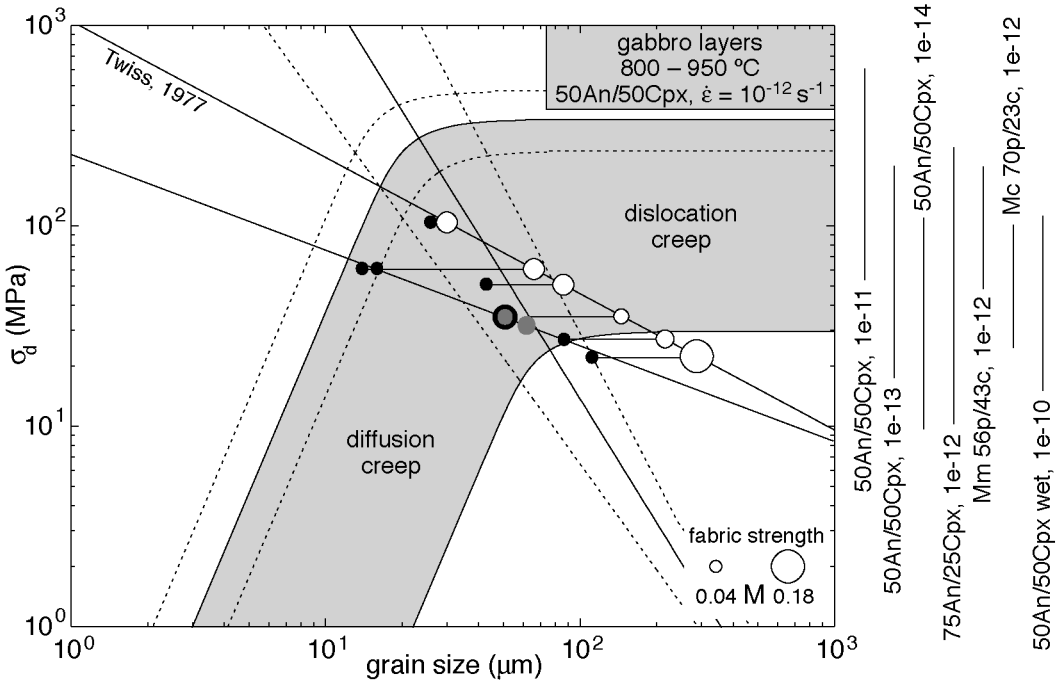

Figure 12. Deformation mechanism map comparing a gabbro flow law and SWIR gabbro mylonite layers. The flow law curves are calculated with the 50An/50Cpx parameters from Dimanov and Dresen [2005], at a strain rate of 10^{-12} s^{-1} and at temperatures of 800 and 950 °C (high and low stress contour, respectively). The dislocation creep stresses for dry and wet gabbros at the same temperature range but different strain rates are shown to the right of the plot, see text for references. Errors associated with Q and n are shown by the dashed lines at the 800 °C contour and the boundary separating the diffusion and dislocation creep fields. Gabbro mylonite layers are plotted as solid symbols at weighted average grain sizes and stress estimates based on neighboring monophase layers. Symbol size is proportional to fabric strength as quantified with the M-index. Gray symbols lack neighboring plagioclase layers and are plotted on the best-fit curve to the solid symbols, see text. Note the fabric strength reduction in all but one plagioclase-gabbro pair.

Figure 13 (next page). Evaluation of monophase and polyphase flow laws at typical SWIR conditions. Stress-strain rate curves are shown for anorthite [*Rybacki and Dresen*, 2000], and gabbro [50An/50Cpx parameters, *Dimanov and Dresen*, 2005]. The shaded region around the curves represents the error in Q and n. The geologically constrained stress and strain rate are shown by the open box. Deformation dominated by dislocation creep is parallel to the $n = 3$ line. Deformation dominated by diffusion creep is parallel to the $n = 1$ line. Circles indicate dislocation creep strain rates for Columbia (c, 70% plagioclase) and Maryland (m, 56% plagioclase) diabase [*Mackwell*, 1998] at a given stress. a) T = 875 ºC. Grain sizes are based on the piezometric relationship (Figures 11 and 12) at a stress of 50 MPa: anorthite = 100 μm, gabbro mylonite = 35 μm, coarse gabbro = 3000 μm. b) T = 925 ºC. At the assigned stress of 20 MPa, we use grain sizes of: anorthite = 300 μm, gabbro mylonite = 100 μm, coarse gabbro = 3000 μm. At these conditions the polyphase strain rate is underestimated. The anorthite and polyphase laws are in better agreement at 875 and 925 ºC if the grain size exponent, p, is assigned a value of 2.4 for gabbro (diffusion creep).

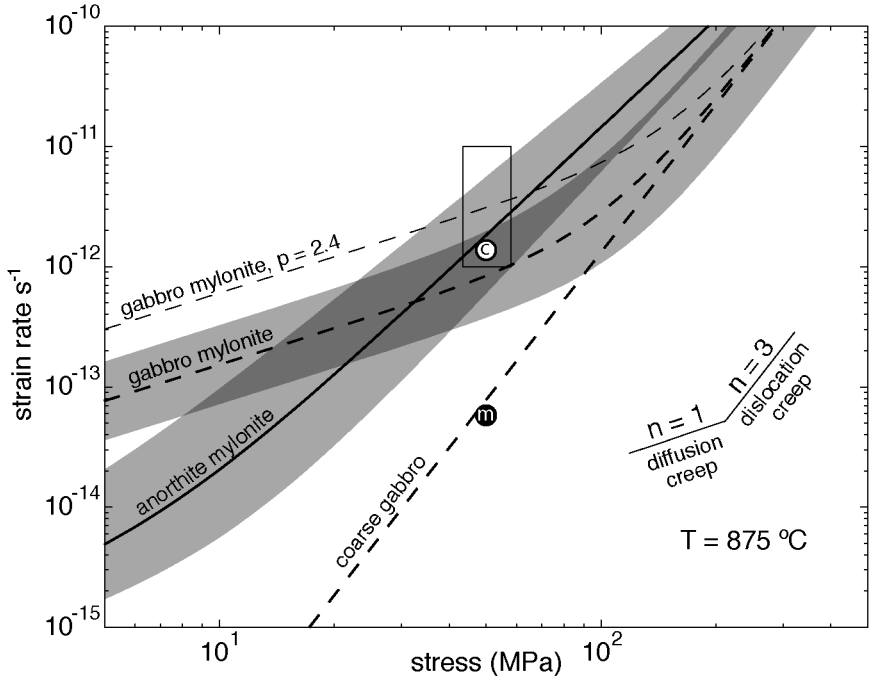
strain rate s-1
10-10
10-11
10-12
10-13
10-14
10-15
gabbro mylonite, p = 2.4
gabbro mylonite
anorthite mylonite
coarse gabbro
c
m
n = 1
diffusion creep
n = 3
dislocation creep
T = 875 ºC
10^1
10^2
stress (MPa)

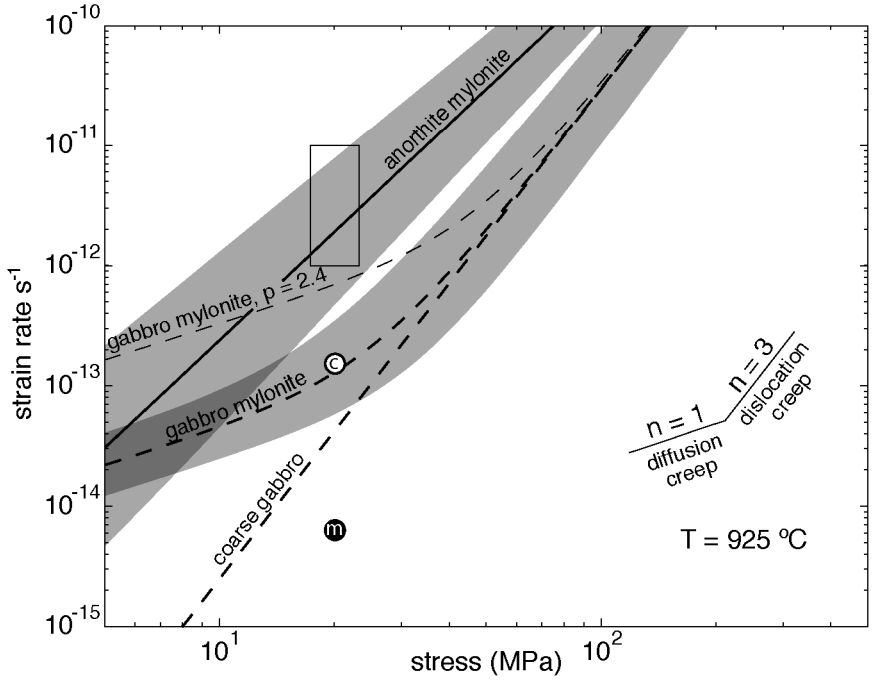
strain rate s-1
10-10
10-11
10-12
10-13
10-14
10-15
anorthite mylonite
gabbro mylonite, p = 2.4
gabbro mylonite
coarse gabbro
c
m
n = 1
diffusion creep
n = 3
dislocation creep
T = 925 ºC
10^1
10^2
stress (MPa)

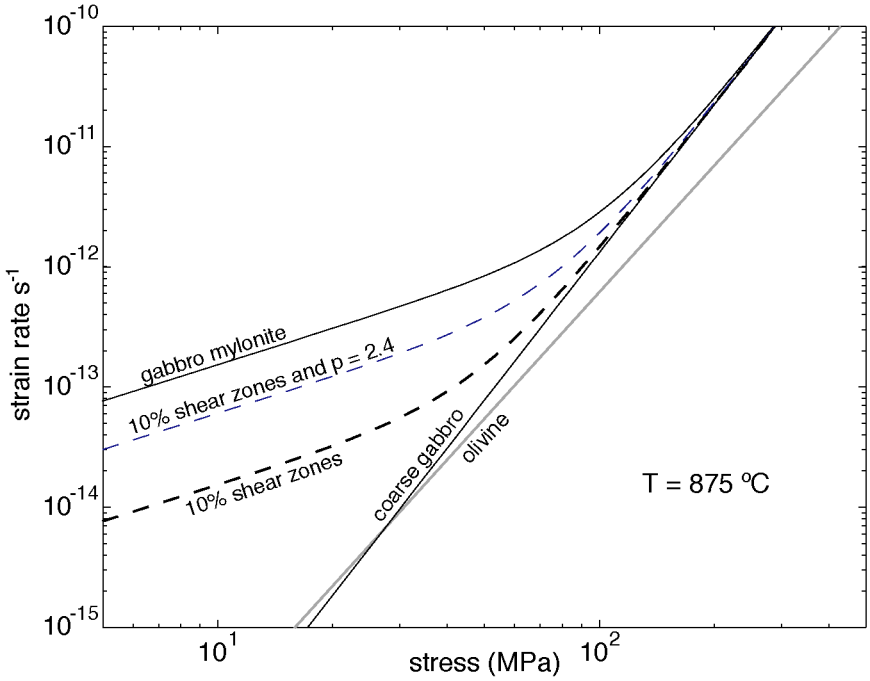

Figure 14. Crustal weakening due to shear zones. Stress-strain rate curves are shown for coarse gabbro and gabbro mylonite (3000 µm and 35 µm, respectively, 50An/50Cpx from Dimanov and Dresen, 2005), dry olivine (3000 µm, from Hirth and Kohlstedt, 2003) and a crustal section with 10% shear zones (as constrained by structural observations of the SWIR gabbros). At a stress of 50 MPa, the strain rate of gabbroic crust with 10% shear zones (~$2x10^{-13}$ s^{-1}) is about twice as fast as that for a gabbroic crust without shear zones. The strain rate is another factor of two times faster if the grain size exponent, *p*, is assigned a value of 2.4 in the diffusion creep flow law.

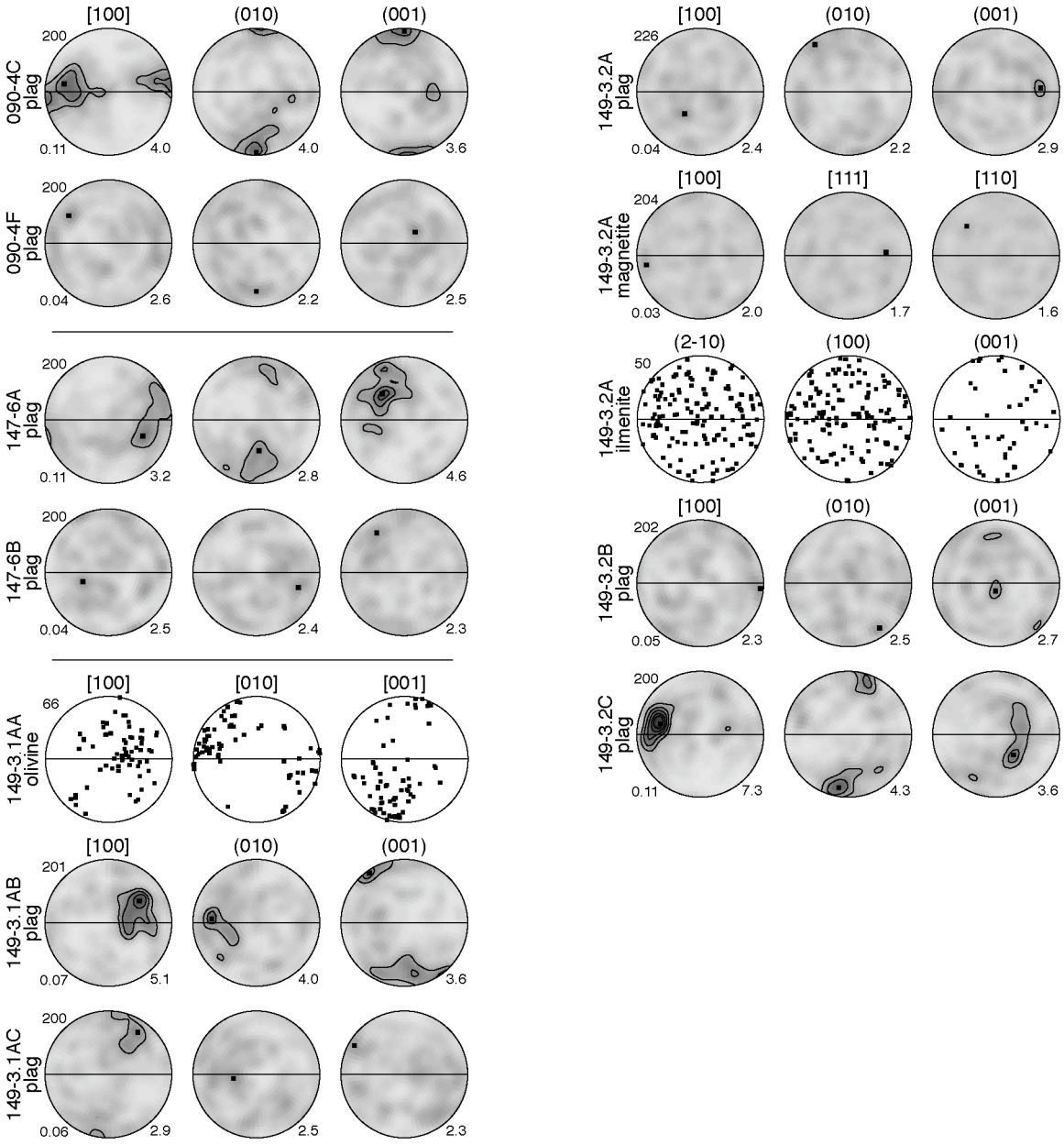

Figure A1. Pole figures for plagioclase (plag), olivine, clinopyroxene (cpx), magnetite, and ilmenite for shear zones 090-4, 147-6, 149-3.1, and 149-3.2. Refer to Figure 6 for plotting conventions and Table 1 for microstructure data. The pole figure in 149-3.2C shows a host-controlled relationship with porphyroclast 149-3.2D in Figure A3.

Figure A2 (next page). Pole figures for plagioclase (plag), olivine, and clinopyroxene (cpx), for shear zones 155-1 188-3.2A and 188-3.2B. Refer to Figure 6 for plotting conventions and Table 1 for microstructure data. Layer 155-1C is the only analyzed monophase mylonite layer with a weak LPO. This layer is separated into four 50 grain domains to illustrate the spatial change in orientations. The combined fabric (sum) illustrates shows the weak total fabric. Layer 155-1D is the only analyzed gabbro mylonite layer with a strong LPO.

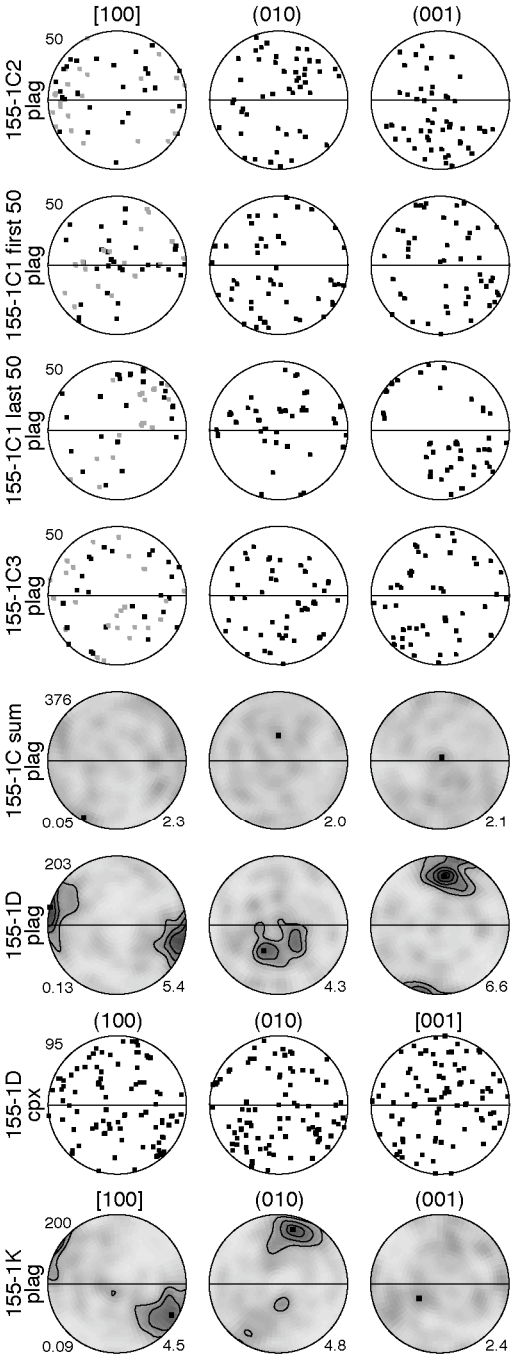
[100]
(010)
(001)
155-1C2 plag
50
155-1C1 first 50 plag
50
155-1C1 last 50 plag
50
155-1C3 plag
50
155-1C sum plag
376
0.05
2.3
2.0
2.1
155-1D plag
203
0.13
5.4
4.3
6.6
(100)
(010)
[001]
155-1D cpx
95
[100]
(010)
(001)
155-1K plag
200
0.09
4.5
4.8
2.4

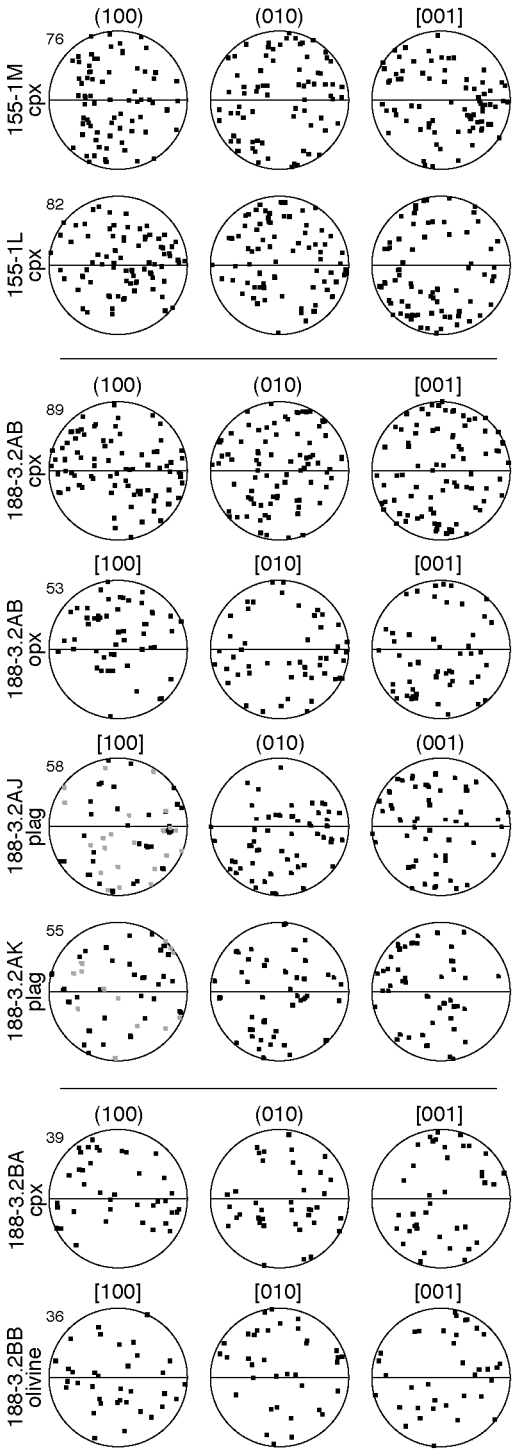
(100)
(010)
[001]
155-1M cpx
76
155-1L cpx
82
188-3.2AB cpx
89
[100]
[010]
[001]
188-3.2AB opx
53
188-3.2AJ plag
58
(001)
188-3.2AK plag
55
188-3.2BA cpx
39
188-3.2BB olivine
36

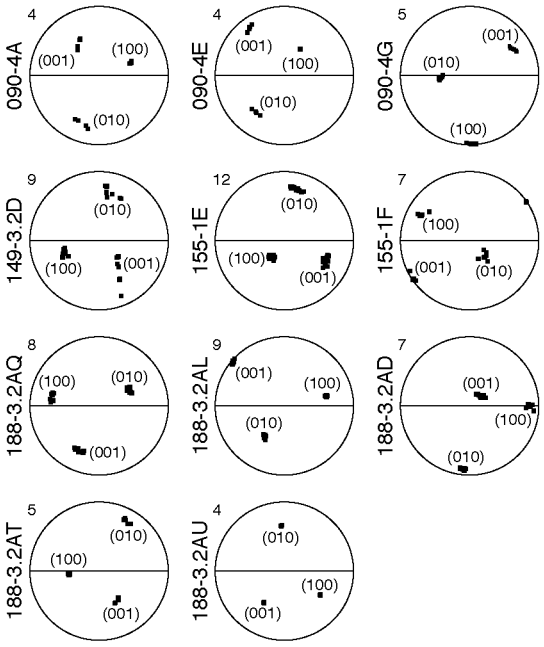

Figure A3. Pole figures for subgrains within porphyroclasts. Refer to Figure 8 for plotting convention.